AIAA AVIATION Forum
June 27-July 1, 2022, Chicago, IL & Virtual
AIAA AVIATION 2022 Forum

10.2514/6.2022-3949

Numerical Analysis of Carbon-based Nozzle Erosion including Transient Heating and Shape Change

Marco Rotondi*, Mario Tindaro Migliorino† and Daniele Bianchi‡
Sapienza University of Rome, 00184 Rome, Italy

Nozzle erosion during solid rocket motors and hybrid rocket engines firings needs to be accurately predicted in order to get reliable performance predictions. Moreover, the accurate sizing of the ablative thermal protection system (TPS), ensuring lightweight (i.e., minimum thickness) structures and preventing excessive heating, is of fundamental importance. In this context, reliable numerical models are required to accurately predict the thermochemical and thermophysical behavior of ablative TPS. The aim of the present work is to perform a numerical investigation on the coupled effects of nozzle ablation and of its thermophysical material response. This is achieved by performing axisymmetric computational fluid dynamics (CFD) simulations including finite-rate ablative boundary conditions and simulations obtained with the recently developed Porous material Analysis Toolbox based on Open-FOAM (PATO). Finite-rate thermochemical ablation tables for propulsive nozzle applications are firstly generated and then provided to PATO. The main advantages of employing these finite-rate tables are highlighted by comparison with the classical chemical equilibrium approach. The results obtained by loosely coupling CFD and material response simulations (using both finite-rate and equilibrium ablation tables) are validated by comparison with firing tests data of a sub-scale Space Shuttle solid propellant booster employing a carbon-phenolic nozzle.

I. Introduction

Carbon-based ablative materials are commonly used in propulsive nozzles of solid rocket motors (SRM) and hybrid rocket engines (HRE) as thermal protection systems (TPS) because of their excellent thermal and physical properties. The carbon-based nozzle surface recedes because of the chemical and mechanical interaction with the hot exhaust gases, increasing the nozzle throat area and resulting in a performance loss. The description and modeling of the major physical mechanisms governing the erosion and the thermophysical behavior of the TPS are therefore of fundamental importance.

The historical approach to ablative response modeling, which was used for re-entry applications since the 50's, was based on the decoupled analysis of the external flow field and of the in-depth material response (MR). Moreover, the MR analysis was carried out by using semi-empirical correlations and employing the equilibrium thermochemical B′ tables in order to model the surface chemical reactions, and typically assuming one-dimensional heat conduction and pyrolysis [1].

The recent use of ablative finite-rate boundary conditions in CFD codes [2–5] introduces the possibility to perform high-fidelity coupled ablative simulations without the requirement of a MR software, allowing to take into account more rigorously geometrical, boundary-layer, and chemical kinetics effects on the ablative response, obtaining quite reliable results in both diffusion and kinetic-limited ablation regimes. However, such CFD gas-surface interaction boundaries are normally computed assuming one-dimensional steady-state conduction into the solid surface, hence neglecting transient and multi-dimensional effects in the material response, which may have a relevant role. Hence, in order to correctly capture multi-dimensional and transient effects, CFD ablative codes must be coupled to multi-dimensional MR softwares. Different MR codes, specific for the analysis of TPS materials subjected to high-enthalpy flows, have been developed recently [6], by upgrading the original one-dimensional CMA (Charring Materials Ablation) model [1].

Different works have faced the problem of CFD-MR coupling in order to predict ablative TPS behavior under high-enthalpy flow conditions. Most investigates re-entry capsule applications [7–11] while just a few deal with propulsive applications limited to SRM [12, 13]. Instead, the problem of nozzle ablation in HRE is still the subject of

*PhD Student, Department of Mechanical and Aerospace Engineering, Via Eudossiana 18, Member AIAA, corresponding author, marco.rotondi@uniroma1.it
†Research Fellow, Department of Mechanical and Aerospace Engineering, Via Eudossiana 18, Member AIAA.
‡Associate Professor, Department of Mechanical and Aerospace Engineering, Via Eudossiana 18, Member AIAA.

different numerical and experimental research activities [14–17], and a detailed CFD-MR coupled analysis of HRE is still missing in the literature. It is worth noting how MR codes have been historically developed in order to be used mainly in re-entry application analysis. In fact, those codes employ the equilibrium B' thermochemical tables and heat and mass transfer coefficients in order to model the surface chemical reactions. The assumption of chemical equilibrium at surface during the ablation process is valid when a diffusion-limited ablation regime is ensured, which is almost always the case of re-entry capsule applications. On the other hand, when a kinetic-limited ablation regime is established, finite-rate effects must be carefully taken into account. This is the case of most propulsive nozzle applications ranging from HRE to SRM (for the latter, especially in case of low contents of metallic powders [3]). This is the main reason why nowadays MR codes are not largely used for propulsive nozzles ablative analysis.

In this context, the present work is aimed to the establishment of an effective ablative CFD-MR loosely coupled analysis in propulsive nozzles. The CFD code used is an in-house code including finite-rate ablative boundary conditions. The selected MR software to be loosely coupled to the CFD code is PATO (Porous material Analysis Toolbox based on Open-FOAM) [18], a recently developed and innovative 3D material response code used in literature for the analysis of re-entry capsules [19]. Re-entry applications have been already analyzed by the author loosely coupling the two aforementioned codes [20]. The obtained results have shown how the coupling strategy adopted seems to be promising, encouraging its extension to propulsive nozzles. However, it is worth noting how the already available ablative models in PATO are limited to re-entry applications (i.e., carbon-phenolic ablators in air). Hence, in order to extend the analysis towards propulsive nozzles, the required B' thermochemical tables (depending on the particular propellants considered) must be generated and provided to the MR code. However, as the equilibrium approach is known to be generally unreliable in propulsive nozzle applications, finite-rate effects must be taken into account when computing the B' tables. In order to do this, a specific routine for the generation of finite-rate B' tables for propulsive nozzles has been implemented. The final goal is to prove the validity of the CFD-MR coupling strategy developed and compare results obtained using both the equilibrium and the finite-rate B' thermochemical tables. The numerical procedure will be validated by comparison with the experimental data available from two different firing tests of the High Internal Pressure–Producing Orifice (Hippo) motor [21], a sub-scale Space Shuttle solid propellant booster employing a carbon-phenolic nozzle.

II. Theoretical and Numerical Model

In this work, the three-dimensional Navier-Stokes equations for compressible, non-reactive, single-phase flows, including variable thermodynamic and transport properties, are solved with a parallel code. The code employs a standard second-order finite volume Godunov formulation. The viscous fluxes are approximated by central differences, whereas the convective fluxes are computed through the solution of Riemann problems whose left and right states are reconstructed by an interpolation procedure using the minmod limiter. The system of ordinary differential equations is advanced in time by means of an explicit third-order Runge-Kutta integration. The solver has been fully integrated with a customized gas-surface interaction (GSI) wall boundary condition with heterogeneous finite-rate surface chemistry for carbon-based ablators, which allows to compute the ablation mass blowing flux, the surface chemical composition, and the surface temperature as part of the CFD steady-state solution. The numerical tool has been validated for pyrolyzing and non-pyrolyzing ablative materials [22–31].

The aforementioned CFD code has been loseely coupled to a material response code. The selected material response code is PATO [32, 33], which is able to compute the temperature evolution of three-dimensional pyrolizing porous materials. PATO solves jointly the mass, momentum, and energy governing equations in volume-averaged form by means of an implicit first-order scheme [33]. Thanks to the inclusion of the momentum conservation equation in PATO, both the magnitude and the direction of the pyrolysis gases velocity vector are computed, representing an important step forward with respect to typical one-dimensional material response codes [1]. Within the software, ablation is accounted for under the thermochemical equilibrium assumption by using the so-called B' tables, as done in most of the material response tools currently available in the open literature [34]. However, a specific numerical routine able to compute finite-rate B' tables has been derived in this work, as the equilibrium assumption is known to be generally unreliable in propulsive nozzle applications. PATO has been largely validated for pyrolyzing ablative materials applications concerning re-entry flights [32, 35, 36], however it has not yet been used for rocket nozzles analysis.

A. CFD - Nozzle Thermochemical Erosion

In the CFD code, the thermochemical ablation of non-pyrolyzing carbon-based materials is modeled via surface mass and energy balances and takes into account heterogeneous chemical reactions at the nozzle surface, rate of diffusion

of the species through the boundary layer, and ablation species injection in the boundary layer. If it is assumed that no material is being removed in a condensed phase (solid or liquid), then the general conservation laws at the gas–solid interface can be written as [22]

$$\text{Mass:} \qquad \dot{m}_{\mathrm{w}} = (\rho v)_{\mathrm{w}} = \rho_{\mathrm{s}} \dot{\mathrm{r}} \tag{1}$$

$$\text{Species:} \qquad \rho D \left.\frac{\partial y_i}{\partial \eta}\right|_{\mathrm{w}} + \dot{\omega}_i = (\rho v)_{\mathrm{w}} y_{i_{\mathrm{w}}} \qquad (i = 1, \ldots, N) \tag{2}$$

$$\text{Energy:} \qquad k \left.\frac{\partial T}{\partial \eta}\right|_{\mathrm{w}} + \sum_{i=1}^{N} h_{i,\mathrm{w}} \rho D \left.\frac{\partial y_i}{\partial \eta}\right|_{\mathrm{w}} + \dot{m}_{\mathrm{w}} h_{\mathrm{s,w}} + q_{\mathrm{rad_{in}}} = q_{\mathrm{cond_w}} + q_{\mathrm{rad_{out}}} + (\rho v)_{\mathrm{w}} h_{\mathrm{w}} \tag{3}$$

where v_{w} stands for the radial velocity in the gas phase due to ablation products injection, the term $\dot{m}_{\mathrm{w}} h_{\mathrm{s,w}}$ is the energy flux entering the surface due to surface recession, while the term $(\rho v)_{\mathrm{w}} h_{\mathrm{w}}$ is the energy flux leaving the surface due to blowing.

Concerning the solid conduction term, it is assumed that the heat conduction is dominant in the direction normal to the nozzle surface. In fact, although tangential temperature gradients certainly exist along the nozzle wall, they are generally negligible if compared to those in the normal direction and are considered a second-order effect. Assuming a steady-state condition, the solid conduction term can be expressed as

$$q_{\mathrm{cond}} = k_{\mathrm{s}} \left.\frac{\partial T_{\mathrm{s}}}{\partial \eta}\right|_{\mathrm{w}} = \dot{m}_{\mathrm{w}} (h_{\mathrm{s,w}} - h_{\mathrm{s},0}) \tag{4}$$

where the term $h_{\mathrm{s},0}$ represents the enthalpy of the material at the initial or undisturbed temperature. Note that the steady-state solid heat conduction flux is only affected by the material specific heat (through the enthalpy difference) and not by its thermal conductivity, which only influences the in-depth solid temperature profile.

Table 1 Heterogeneous rate constants of carbon with H_2O, CO_2, OH, O, and O_2 [37, 38]

Surface reaction	j	A_j	E_j, kJ/mol	b_j	n_j
$C_s + H_2O \Rightarrow CO + H_2$	1	$4.8 \cdot 10^5$	288	0.0	0.5
$C_s + CO_2 \Rightarrow 2\,CO$	2	$9.0 \cdot 10^3$	285	0.0	0.5
$C_s + OH \Rightarrow CO + H$	3	$3.61 \cdot 10^2$	0.0	-0.5	1.0
$C_s + O \Rightarrow CO$	4	$6.655 \cdot 10^2$	0.0	-0.5	1.0
$C_s + \frac{1}{2}O_2 \Rightarrow CO$	5	$2.4 \cdot 10^3$	125.6	0.0	-
	6	$2.13 \cdot 10^1$	-17.17	0.0	-
	7	$5.35 \cdot 10^{-1}$	63.64	0.0	-
	8	$1.81 \cdot 10^7$	406.1	0.0	-

The heterogeneous chemical reactions taking place at the nozzle surface are modeled by the semi-global graphite oxidation kinetics proposed originally by Bradley et al. [37] and then adopted by Chelliah et al. [38] (Table 1). With this mechanism, the contribution to erosion due to the i-th species can be expressed in kg/(m$^2 \cdot$ s) as:

$$\dot{m}_{\mathrm{w},i} = \mathrm{k}_j \mathrm{p}_i^{n_j} \qquad \text{for species } i = \mathrm{H_2O}, \mathrm{CO_2}, \mathrm{OH}, \text{ and } \mathrm{O} \tag{5}$$

$$\dot{m}_{\mathrm{w},i} = \frac{\mathrm{k}_5 \mathrm{p}_i Y}{1 + \mathrm{k}_6 \mathrm{p}_i} + \mathrm{k}_7 \mathrm{p}_i (1 - Y) \qquad \text{where } Y = \left(1 + \frac{\mathrm{k}_8}{\mathrm{k}_7 \mathrm{p}_i}\right)^{-1} \qquad \text{for species } i = \mathrm{O_2} \tag{6}$$

where p_i is the partial pressure (in atm) of the oxidizing species i, n_j is the overall order of the heterogeneous j-th reaction, and k_j is its specific rate constant, which can be expressed by an Arrhenius type expression of the form:

$$\mathrm{k}_j = A_j T_{\mathrm{w}}^{b_j} \exp(-E_j / \Re T_{\mathrm{w}}) \tag{7}$$

where T_{w} is the wall temperature (in Kelvin) and A_j, b_j, and E_j are the pre-exponential factor, the temperature exponent, and the activation energy for the j-th reaction, respectively. The surface reaction rates calculated according to Eqs. (5)

and (6) for varying wall temperature are reported in Fig. 1(a) for a representative partial pressure of 1 atm. The total ablation mass flux of carbon due to the surface heterogeneous reactions is finally expressed as:

$$\dot{m}_{\mathrm{w}} = \dot{m}_{\mathrm{w,H_2O}} + \dot{m}_{\mathrm{w,CO_2}} + \dot{m}_{\mathrm{w,OH}} + \dot{m}_{\mathrm{w,O}} + \dot{m}_{\mathrm{w,O_2}} \tag{8}$$

The rate of production/consumption of the generic gas-phase species i at the nozzle surface $\dot{\omega}_i$ in Eq.(2) can be easily derived from the rate of ablation of carbon by the generic oxidizing species, Eqs.(5) and (6), and the mass balance available once the species molecular weights and the stoichiometry of the surface reactions (see Table 1) are known.

In terms of energy absorbed (or released) by the surface reaction, it is worth noting that the reactions with H_2O, CO_2, and OH are characterized by a positive heat of reaction, which means that energy is absorbed when carbon is oxidized by one of these oxidizing species, whereas the reactions with O_2 and O are characterized by a negative heat of reaction, hence energy is released (see Fig. 1(b)).

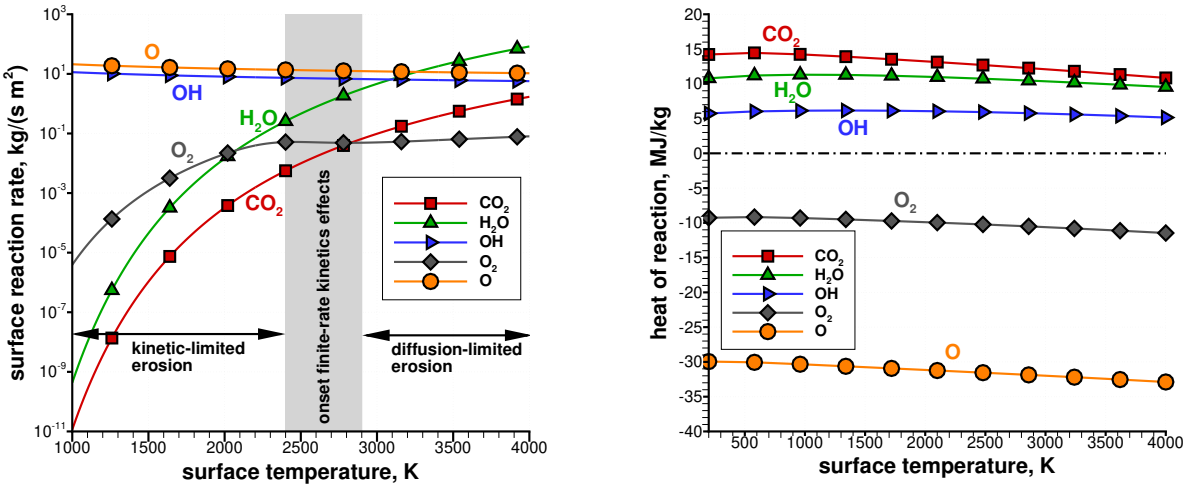

(a) Surface reaction rate at 1 atm.

(b) Heat of reaction per mass of graphite consumed.

Figure 1 Surface reaction rate and heat of reaction of heterogeneous surface reactions.

B. PATO - Transient Heating and Ablation

PATO solves jointly the mass, momentum, and energy governing equations inside a solid medium with boundary conditions obtained from an external flow solver. The code can be used by setting boundary conditions at the surface exposed to the hot gases which impose wall temperature, pressure, and/or recession rate. However, in ablative conditions, wall temperature and recession rate are both unknown, hence the solution of a surface energy balance (SEB) and a surface mass balance (SMB) is needed. The SEB in PATO is similar to the one used in the GSI model (see Eq.(3)) integrated within the CFD solver. The general PATO SEB reads as follows [32]:

$$\begin{aligned} q_{\mathrm{conv}} + q_{\mathrm{diff}} + q_{\mathrm{rad_{in}}} + q_{\mathrm{adv_{in}}} = q_{\mathrm{cond}} + q_{\mathrm{rad_{out}}} + q_{\mathrm{adv_{out}}} \quad \Rightarrow \\ \rho_e u_e C_H (h_r - h_{ew}) + \rho_e u_e C_M (h_{ew} - h_{\mathrm{w}}) + q_{\mathrm{rad_{in}}} + \dot{m}_{pg} h_{pg} + \dot{m}_{ch} h_{ch} = q_{\mathrm{cond}} + \epsilon\sigma T_{\mathrm{w}}^4 + \dot{m}_{pg} h_{\mathrm{w}} + \dot{m}_{ch} h_{\mathrm{w}} \end{aligned} \tag{9}$$

where q_{conv}, q_{diff}, and $q_{\mathrm{rad_{in}}}$ are respectively the convective, diffusive, and radiative incoming heat fluxes from the hot-gas side, $q_{\mathrm{adv_{in}}}$ and q_{cond}, are respectively the heat flux advected and conducted inside the solid material, and $q_{\mathrm{rad_{out}}}$ and $q_{\mathrm{adv_{out}}}$ are respectively the heat flux re-radiated from the solid wall and the heat flux blown away from the surface thanks to the pyrolysis and ablation processes. Moreover, the subscripts ch and pg refer to the ablation phenomenon at surface (i.e., char) and to the in-depth decomposition and pyrolysis processes, respectively.

In the present study, PATO is employed under the typical assumption of unity Lewis number (Le), which, through the Chilton-Colburn relation ($C_{\mathrm{M}} = C_{\mathrm{H}}\mathrm{Le}^{\frac{2}{3}}$), yields $C_{\mathrm{M}} = C_{\mathrm{H}}$. Under the assumption of unitary Lewis number, the SEB

in Eq. (9) can be simplified as follows:

$$q_{\text{cond}} = \rho_e u_e C_H (h_r - h_{\text{w}}) + \dot{m}_{pg}(h_{pg} - h_{\text{w}}) + \dot{m}_{ch}(h_{ch} - h_{\text{w}}) \tag{10}$$

where the incoming radiation from the hot gases, $q_{\text{rad}_{\text{in}}}$, and re-radiation from the solid surface have been neglected. The first term in the right-hand side of Eq.(10) depends on the wall enthalpy (which is evaluated by PATO employing pre-computed thermochemical ablation tables [1]), on the recovery enthalpy, h_r, and on the dimensional heat transfer coefficient, $\rho_e u_e C_H$ (which are both provided by CFD simulations). The dimensionless mass and heat transfer coefficients are computed from CFD data as:

$$\rho_e u_e C_H = \frac{q_{\text{conv}}}{h_r - h_{ew}} = \frac{k \frac{\partial T}{\partial \eta}\big|_{\text{w}}}{h_r - h_{ew}}; \qquad \rho_e u_e C_M = \frac{q_{\text{diff}}}{h_{ew} - h_{\text{w}}} = \frac{\sum_{i=1}^{N} h_{i,\text{w}} \rho D \frac{\partial y_i}{\partial \eta}\big|_{\text{w}}}{h_{ew} - h_{\text{w}}} \tag{11}$$

In particular, the convective and diffusive heat fluxes and the wall enthalpy, h_{w}, are calculated by the CFD code employing an ablative wall boundary condition, while the recovery enthalpy, h_r, is obtained using an adiabatic wall boundary. On the other hand, h_{ew} is computed by a simple CFD post-processing, assuming a frozen chemical composition in the boundary layer and using the wall temperature distribution obtained with the ablative CFD. It is worth noting how, since the CFD considers already the coupling with an ablative wall boundary condition, no blowing correction is needed for the evaluation of the heat flux coefficient C_H within the material response code [1] and the value provided from the CFD code is directly used. This allows to reduce the reliance on semi-empirical correlations typically employed in material response codes and improves the predictive capability of the numerical approach.

Finally, the CFD wall pressure is employed as boundary condition for the momentum equation, which allows to compute the velocity and direction of the pyrolysis gases [18]. More details on the governing equations formulation and ablation/pyrolysis modeling of PATO can be retrieved in [32, 33]. In particular, all the expressions needed for the calculation of the mass flux of pyrolysis gases $\dot{m}_{pg}$ is reported in [32].

C. Thermochemical Ablation Tables

In PATO the evaluation of the ablation mass flux is carried out using the thermochemical B' ablation tables, which simply represent a tabulated solution of the SMB. Those tables are widely widespread under the chemical equilibrium assumption in most material response codes, with specific applications to carbon ablation in air [34]. However, the B' tables are strongly dependent on the environmental gas considered, hence, concerning their extension towards propulsive applications, they have to be derived and implemented within PATO depending on the specific environmental gas (i.e., propellant formulation) to be analyzed. Moreover, chemical kinetic effects need to be included, as they are generally important in propulsive nozzle applications. Therefore, in this work a specific numerical routine has been derived, which is able to compute finite-rate B' tables for carbon-based materials ablation in a generic gaseous environment. The finite-rate B' tables obtained are then compared to the classical chemical equilibrium ones, highlighting their main advantages and additional features.

1. Chemical Equilibrium Tables

In the most general case including in-depth decomposition and pyrolysis, the B' parameter (or dimensionless ablation mass flux parameter) is defined as follows [1]:

$$B' = B'_{ch} + B'_{pg}; \qquad B'_{ch} = \frac{\dot{m}_{ch}}{\rho_e u_e C_M}; \qquad B'_{pg} = \frac{\dot{m}_{pg}}{\rho_e u_e C_M} \tag{12}$$

By using these definitions, under the hypotesis of chemical equilibrium at surface, the SMB can be expressed as:

$$(Y_{k_e} - Y_{k_{\text{w}}}) + B'_{ch} Y_{k_{ch}} + B'_{pg} Y_{k_{pg}} = (B'_{ch} + B'_{pg}) Y_{k_{\text{w}}} \tag{13}$$

where Y_k are the equilibrium elemental mass fractions and k represents the k-th chemical element. Considering a carbon-based ablative material, carbon is the only chemical element at surface (i.e., $k = C$ and $Y_{C_{ch}} = 1$). Therefore, the following expression for the B' surface ablation parameter (i.e., B'_{ch}) is obtained:

$$B'_{ch} = \frac{Y_{C_{\text{w}}} - Y_{C_e} - B'_{pg}(Y_{C_{pg}} - Y_{C_{\text{w}}})}{1 - Y_{C_{\text{w}}}} \tag{14}$$

from Eq.(14) it is evident how the carbon elemental mass fractions at wall Y_{C_w}, at the boundary-layer edge Y_{C_e}, and in the pyrolysis gases $Y_{C_{pg}}$ are needed for the evaluation of the B' parameter. These elemental mass fractions are evaluated at varying wall temperature, wall pressure, and B'$_{pg}$ by using a specific numerical routine based on the Chemical Equilibrium with Applications (CEA) code [39].

2. Finite-Rate Tables

The SMB considering finite-rate chemistry effects at surface and using the B' parameter definitions in Eq.(12) can be expressed as follows:

$$(y_{i_e} - y_{i_w}) + \frac{\dot{\omega}_i}{\rho_e u_e C_M} + B'_{pg} y_{i_{pg}} = (B'_{ch} + B'_{pg}) y_{i_w} \tag{15}$$

where y_i are the species mass fractions and i indicates the i-th chemical species. From Eq.(15), the following general expression for the B' surface ablation parameter B'$_{ch}$ is obtained for a carbon-based material including in-depth pyrolysis:

$$B'_{ch} = \frac{y_{i_w} - y_{i_e} - \frac{\dot{\omega}_i}{\rho_e u_e C_M} - B'_{pg}(y_{i_{pg}} - y_{i_w})}{y_{i_w}} \tag{16}$$

From Eq.(16) it is evident how the finite-rate B' parameter is not dependent only on the chemical compositions (i.e., on y_{i_w}, y_{i_e}, and $y_{i_{pg}}$, therefore on wall temperature and pressure) and on the pyrolysis process (i.e., on the B'_{pg} parameter), as seen previously in case of the chemical equilibrium assumption (see Eq.(14)). In fact, B'_{ch} is also dependent on the

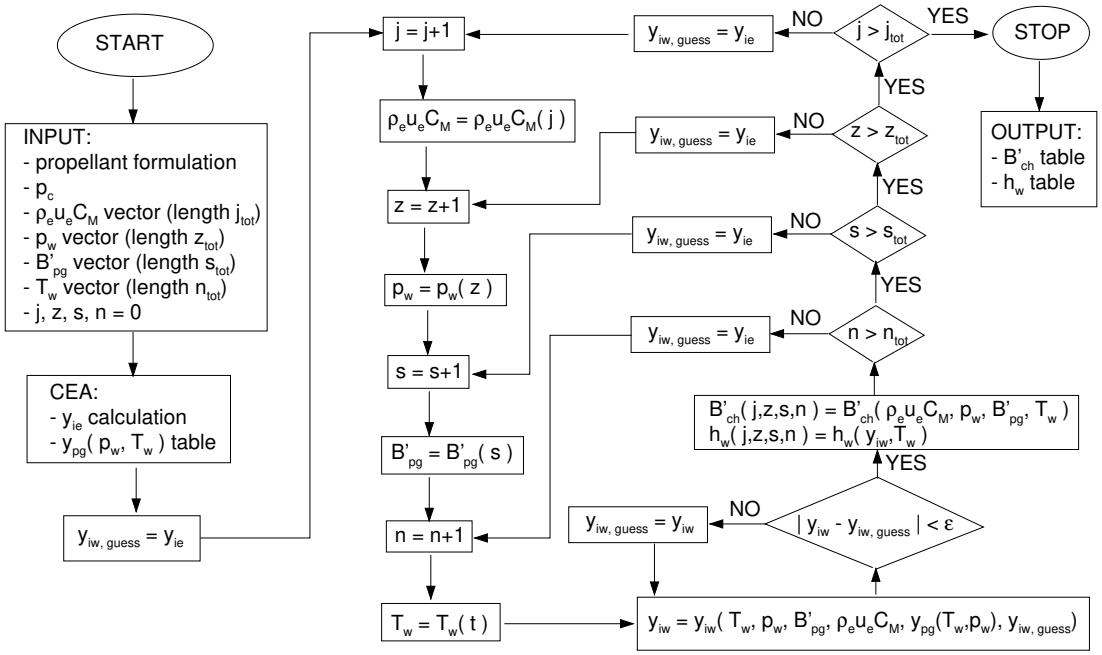

Figure 2 Schematic of the numerical procedure adopted for the calculation of the finite-rate B' tables.

ratio between the heterogeneous surface reaction rates $\dot{\omega}_i$ and the dimensionless mass transfer coefficient $\rho_e u_e C_M$ (third term at numerator in Eq.(16)). This ratio is important as it is able to take into account for the temperatures needed for the establishment of a kinetic or diffusion-limited ablation regime. The heterogeneous surface reactions considered for the calculation of $\dot{\omega}_i$ are the same employed in the CFD ablative boundary condition for carbon ablation (see Table1 and Eqs.(5), (6), and (8)). The numerical procedure employed for the calculation of the finite-rate B' tables is based on the coupling between the CEA code [39] and the finite-rate reaction mechanism [37]. In particular, the wall mass fractions y_{i_w} represent the unknowns of the problem and are calculated in an iterative way starting from a first guess solution. The boundary-layer edge species mass fractions y_{i_e} are used as the first guess solution, and they are calculated from the knowledge of the propellant formulation using the CEA code. The iterative numerical procedure is summarized in details in the schematic reported in Fig.2. In particular, dimensionless mass transfer

coefficient, wall pressure, B'$_{pg}$ parameter, and wall temperature vectors of free lengths are provided as input and iterated in order to obtain a B'$_{ch}(\rho_e u_e C_M, p_w, B'_{pg}, T_w)$ reference mapping function. In order to do this, the solution of the SMB given by Eq.(15) in terms of y_{i_w} is calculated by iterating on the first guess solution. This is possible thanks to a linearization of Eq.(15) around the first guess solution by using taylor expansions, which allows to remove non-linearities. Once the y_{i_w} at the current $\rho_e u_e C_M, p_w, B'_{pg}$ and T_w are obtained, the correspondent B'_{ch} parameter and h_w are computed. During numerical simulations, PATO linearly interpolates inside the obtained $B'_{ch}(\rho_e u_e C_M, p_w, B'_{pg}, T_w)$ and $h_w(\rho_e u_e C_M, p_w, B'_{pg}, T_w)$ tables using the current $\rho_e u_e C_M, p_w, B'_{pg}$ and T_w values.

An example of B' tables, generated under both the hypothesis of chemical equilibrium and with finite-rate chemistry effects, is reported in Fig.3 for a metallized SRM propellant composed by 12% of PBAN (PolyButadiene AcryloNitrile copolymer), 2% of an epoxy curing agent, 70% of AP (ammonium perchlorate), and 16% of aluminum powder. Looking to Fig.3(a), the equilibrium B' parameter shows a practically zero value (i.e., no ablation) at low wall temperatures, a sudden rise around 1000 K, and a constant value (i.e., plateau value) in the range of temperatures between 1500 and 3400 K (surface oxidation). This constant value denotes a diffusion-limited ablation regime starting from 1500 K in case of the equilibrium B' tables. The B' parameter is then increasing for wall temperatures above 3400 K due to carbon sublimation [1]. As expected, the equilibrium B' is not affected by the dimensionless mass transfer coefficient, while it is the case of the finite-rate B' tables. From the finite-rate B' distibutions shown in Fig.3(a), it is evident how the

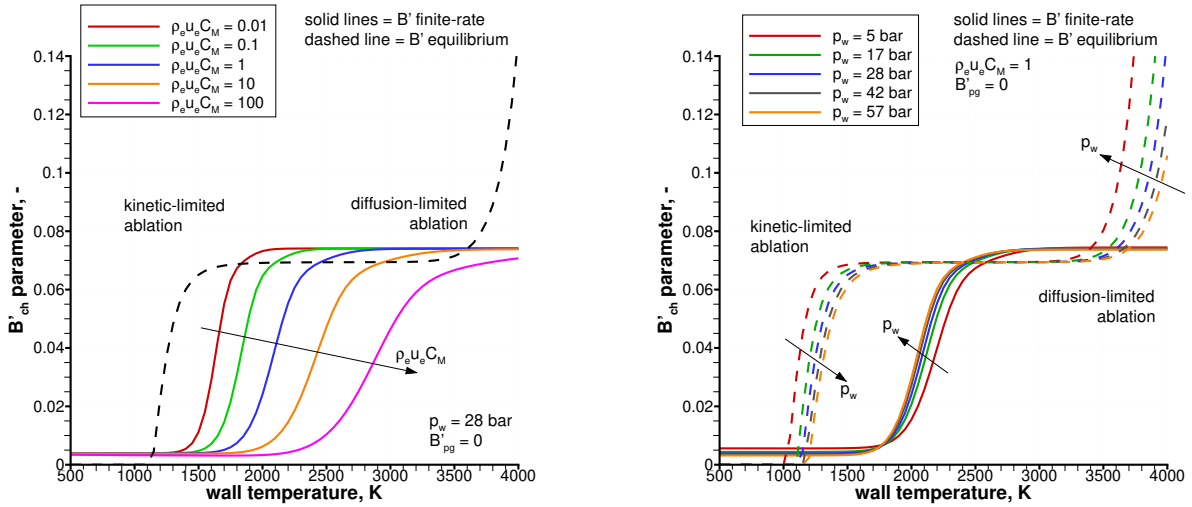

(a) B'$_{ch}$ vs dimensionless mass transfer coefficient.

(b) B'$_{ch}$ vs wall pressure.

Figure 3 Chemical equilibrium vs finite-rate B' ablation tables for a SRM propellant for different dimensionless mass transfer coefficients (i.e., different species diffusion velocities) and different wall pressures.

range of temperatures leading to the transition from kinetic-limited to diffusion-limited ablation regime is not fixed and is affected by the dimensionless mass transfer coefficient. Differently from the chemical equilibrium case, at low temperatures the finite-rate B' parameter is constant and slightly different from zero due to the reactions between carbon and OH and O, which are characterized by a high reaction rate even at low temperature (see Fig.1(a)). Approaching temperatures above 1500-2000 K, the B' parameter grows due to the increase of the reaction rates of carbon with H_2O, CO_2 and O_2 (see Fig.1(a)), denoting a region in which a kinetic-limited ablation is taking place. Then, a constant plateau value is reached, which is close to the equilibrium B' table one, at temperature ranging from 2000 to more than 3500 K depending on the dimensionless mass transfer coefficient, denoting the establishment of a diffusion-limited ablation process. Differently from the equilibrium tables, finite-rate ablation tables are then not increasing for wall temperatures above 3400-3500 K, as carbon sublimation is not included in the finite-rate reaction mechanism adopted (see Table 1). Anyway, carbon sublimation is normally not activated in propulsive applications as wall temperatures are always well below 3400-3500 K even when steady-state are reached. Looking to Fig.3(b), the effect of wall pressure on the B' tables is reported. Concerning finite-rate tables, wall pressure leads to a slightly anticipated transition to the diffusion-limited ablation regime. The reason is the increase of the surface reaction rates as pressure grows (see Eq.(5)). On the other hand, the opposite effect is reported in case of the B' equilibrium tables. Anyway, its physical meaning is

not related to kinetic or diffusion-limited ablation, but only to the role of pressure on the chemistry, slightly altering the wall chemical equilibrium mass fractions at low temperatures.

III. Test Case and Numerical Set-Up

In this work we consider two different firing tests of the Hippo motor [21], a sub-scale Space Shuttle solid propellant booster employing a carbon-phenolic nozzle. Two different scales have been considered, including a 6.35 cm throat diameter (i.e., Hippo 1) and a 17.78 cm throat diameter (i.e., Hippo 2) nozzle. For these nozzles, a large quantity of experimental data are available, including surface recession and char penetration depth as a function of axial position. Detailed information on the propellant formulation and on the ablative material employed are provided in [21]. In particular, the solid propellant is composed by 12% of PBAN (PolyButadiene AcryloNitrile copolymer), 2% of an epoxy curing agent, 70% of AP (ammonium perchlorate), and 16% of aluminum powder. Nozzle material is carbon-phenolic MX-4926, with a virgin density, ρ_v, of 1462 kg/m^3 and a char density, ρ_{ch}, of 1173 kg/m^3 (i.e., $\phi = \frac{\dot{m}_{pg}}{\dot{m}_{ch}} = 0.246$ at steady-state conditions [26]).

The nozzle schematics and the computational set-up used in the numerical simulations are reported in Fig.4. The nozzle contour has been represented by one circular segment, a parabolic segment, and a line segment, whit the following expressions:

$$y = \begin{cases} \sqrt{-x^2 - 5.752\ D_{th}\ x - 6.1949\ D_{th}} & -2.8760\ D_{th} \le x \le -2.0976\ D_{th} \\ D_{th}/0.0635\ (2.5533\ x^2 + 0.03175) & -2.0976\ D_{th} \le x \le 0.8263\ D_{th} \\ D_{th}/0.0635\ (0.2679\ x + 0.02472) & 0.8263\ D_{th} \le x \le 3.6000\ D_{th} \end{cases} \tag{17}$$

The circular arc has been used in order to replace the nose-like geometry at inlet typical of SRM submerged nozzles

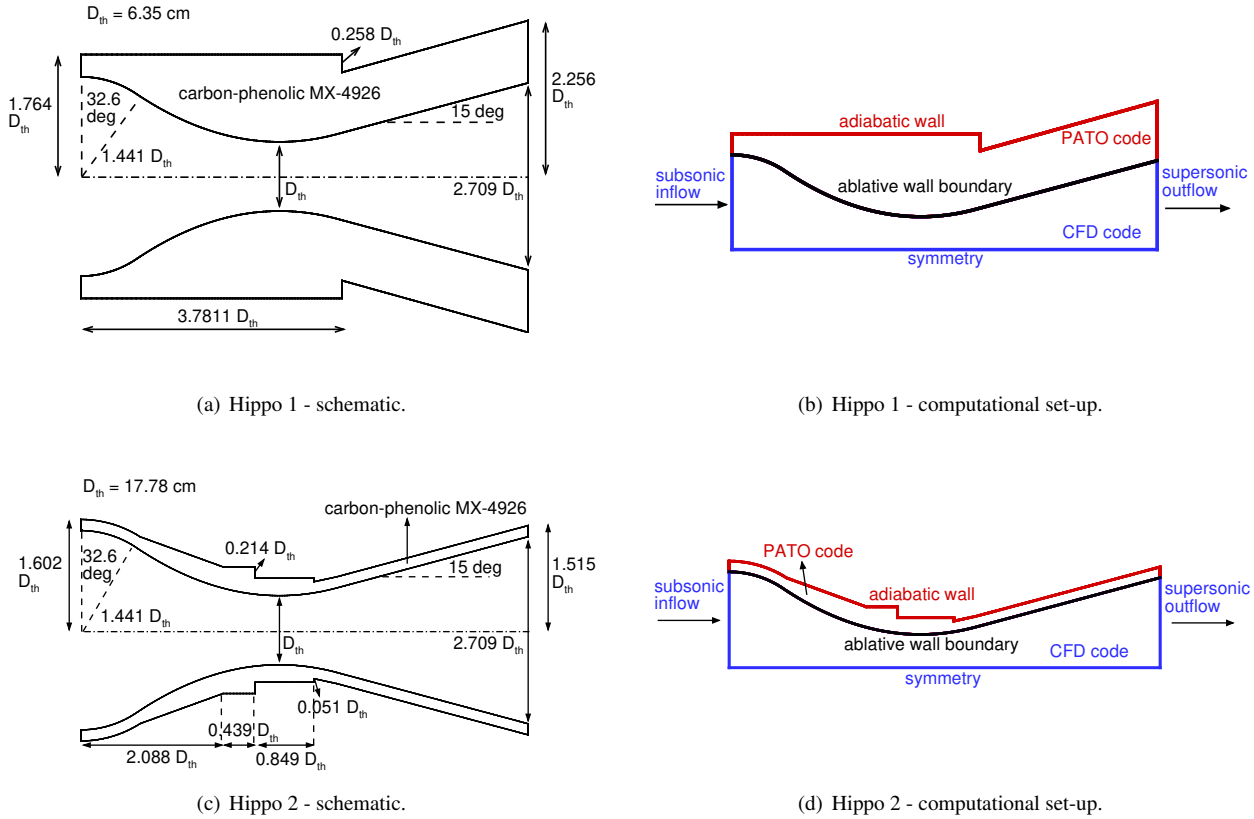

(a) Hippo 1 - schematic.

(b) Hippo 1 - computational set-up.

(c) Hippo 2 - schematic.

(d) Hippo 2 - computational set-up.

Figure 4 Schematics of the Hippo motors and correspondent computational set-ups for the CFD-PATO simulations.

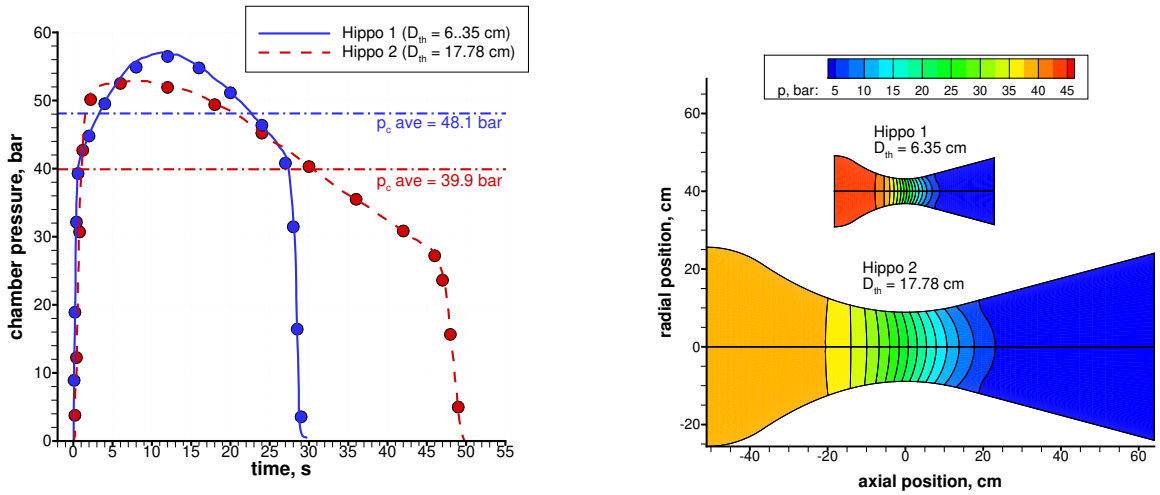

(a) Pressure traces.

(b) Pressure flow fields.

Figure 5 Experimental pressure traces for the two Hippo motor firings under investigation and correspondent pressure flow fields at their average operative chamber pressure.

[21]. In fact, this particular geometry would have caused a certain ambiguity in imposing the inflow boundary condition due to the unknown velocity direction at the inlet. By using the circular arc, the nozzle profile become parallel to the nozzle axis at the inlet section so that an axial inlet velocity profile can be assigned. Since the length of the wall is important because it affects the boundary layer thickness and hence the heat and mass transfer rate, the total wall length of the real entrance profile has been retained. This approximation has shown to be a reasonable choice in different past works [3, 31, 40].

In the CFD side of the computational domain (see the blue zone in Figs.4(b) and 4(d)), boundary conditions other than an ablating wall are enforced as follows: total temperature, total pressure, Mach number, and chemical composition at the inflow (subsonic inlet), no assigned conditions at the outflow (supersonic outlet), and symmetry axis. The numerical simulations assume frozen chemical composition in the flow field. Combustion chamber conditions, used in the subsonic inlet boundary, have been obtained by the Chemical Equilibrium with Applications (CEA) code [39]. Thirteen species (AlOH, Al_2O_3, CO, CO_2, Cl, H, H_2, HCl, H_2O, N_2, O, O_2, OH) have been considered for each equilibrium simulation as they constitute more than 99.9% of the total combustion gas mass for the propellant combination here analyzed. In the CFD simulations, the condensed species Al_2O_3 has been treated as an additional gaseous species in order to simplify the gas-particles mixture modeling, employing the heavy-gas approximation [30]. On the other hand, in the numerical domain for the material response transient simulations (see red zone of Figs. 4(b) and 4(d)), boundary conditions include an ablating front wall, enforced by using CFD-provided inputs (as described in Sec. II.B) and an adiabatic back wall. The solid material temperature at the initial time is assumed to be 298.15 K.

Figure 5(a) presents the Hippo motor chamber pressure time histories for the two nozzles analyzed [21] jointly with the correspondent average p_c values. It is worth noting how the two motor firings considered are quite different not only from the geometrical point of view, but also in terms of operative conditions (see Fig.5(b)). In particular, concerning the Hippo 1 motor, test duration is 29.5 seconds, whit an average operative chamber pressure of 48.1 bar. On the other hand, Hippo 2 motor firing last longer, reaching 49.5 seconds of duration, with a low average chamber pressure of 39.9 bar (see Fig.5(a)). Each pressure trace has been subdivided in a certain number of intermediate points (red and blue dots). These points are needed for the numerical simulation of the nozzle shape change process, as it will be explained in details later. Flow conditions at nozzle inlet obtained using the average chamber pressures are summarized in Table2 for both Hippo 1 and Hippo 2 nozzles. It is worth noting how the two different average chamber pressures are only slightly affecting both combustion products mass fractions and flame temperature. O and O_2 mass fractions have not been reported in Table2 as they are lower than 5e-4. However, they have been included in the numerical simulations as they are included in the surface heterogeneous reactions leading to nozzle ablation (see Table1).

Table 2 Nozzle inlet flow conditions at average chamber pressure conditions.

Test	T_c, K	y_{AlOH}	$y_{Al_2O_3}$	y_{CO}	y_{CO_2}	y_{Cl}	y_H	y_{H_2}	y_{HCl}	y_{H_2O}	y_{N_2}	y_{OH}
Hippo 1	3436	0.008	0.293	0.247	0.025	0.018	0.002	0.020	0.199	0.094	0.088	0.006
Hippo 2	3419	0.008	0.293	0.247	0.025	0.019	0.002	0.020	0.198	0.094	0.088	0.006

IV. Results

A. CFD Results - Steady-State Ablation

In this section, results in terms of nozzle erosion and shape change, obtained using steady-state CFD simulations only, are shown for both Hippo 1 and Hippo 2 nozzles. Firstly, CFD ablative simulations at average chamber pressure conditions have been performed in order to underlines the main differences between the two firing tests considered. Results obtained for the two nozzles are shown in Fig.6. The obtained ablation mass flux distributions are qualitatively similar. However, at throat location the ablation mass flux of Hippo 2 nozzle is 25.8% lower than Hippo 1 one, mainly due to its lower chamber pressure and higher nozzle throat radius. On the other hand, wall temperature distributions are qualitatively and quantitatively similar. In particular, for both nozzles wall temperature is close to 3000 K in the early convergent section (leading to a diffusion-limited ablation regime), then dropping down to 2500 K in the divergent zone (ensuring the transition towards a kinetic-limited ablation regime). Moreover, at throat location, wall temperature for Hippo 2 nozzle is approximately 2740 K, only 1.2% lower than Hippo 1 one. From this single average conditions CFD simulation, a first estimation of the nozzle shape change has been obtained by applying the computed ablation mass flux distributions for the whole firing tests duration. However, by doing so, nozzle shape change effects on the ablation mass flux distributions are not taken into account.

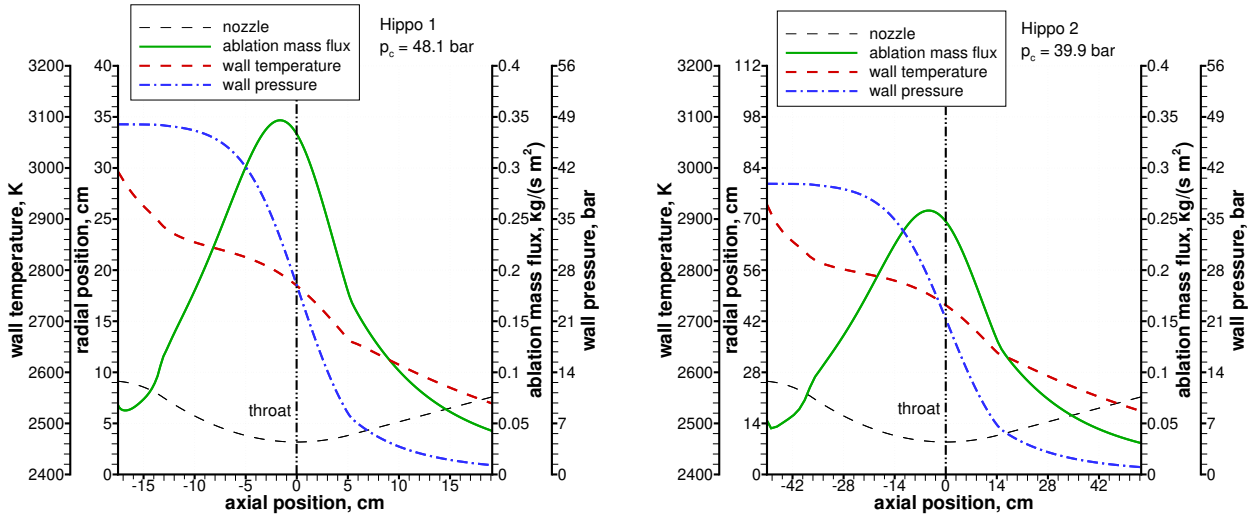

(a) Hippo 1.

(b) Hippo 2.

Figure 6 Ablation mass flux, wall temperature, and wall pressure obtained from steady-state CFD simulations at average chamber pressure conditions for both Hippo 1 and Hippo 2 nozzles.

Therefore, nozzle shape change has been analyzed as well by using subsequent steady-state CFD simulations. In particular, the nozzle geometry has been updated in time in order to include shape change effects on the computed ablation mass flux distributions. CFD simulations are started with the initial shape (see Figs.4(a) and 4(c)), and the surface erosion rate is computed; after that, a specifically implemented shape evolution model is run for a portion of the burning time. Then, a new CFD grid is generated using the receded shape, and a new CFD solution using this grid is computed. Subsequently, the erosion rate distribution is updated, and the procedure is repeated until the total burning time is reached. Each CFD computation is performed at the mean chamber pressure of the corresponding time step, as

reported in Fig.5(a).

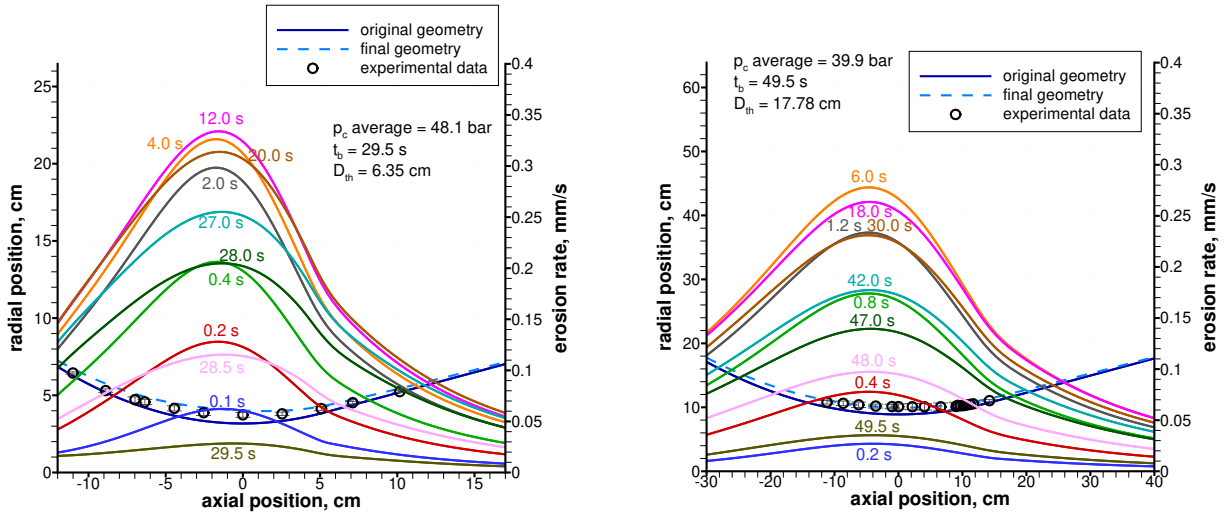

(a) Hippo 1.

(b) Hippo 2.

Figure 7 In-time erosion rate distributions along the nozzle length for the two Hippo motors investigated and resulting nozzle shape change.

Figure 7 shows the erosion rate distributions along the nozzle length at different times obtained according to this numerical procedure. It is worth noting how the erosion rate absolute values along the nozzle are largely changing in time, especially during the first and last few seconds of motors operation. This is the reason why in these phases a reasonably smaller time step has been considered between two subsequent CFD simulations for both motors (see Fig.5(a)). Concerning the Hippo 1 motor firing (see Fig.7(a)), the maximum erosion rate is reported after 12 seconds (i.e., 40.7% of the whole test duration). On the other hand, for the Hippo 2 motor firing (see Fig.7(b)), the maximum erosion rate is reported after just 6 seconds (i.e., 12% of the whole test duration). Moreover, it is worth noting how the Hippo 2 maximum throat erosion rate is 14.7% lower than the Hippo 1 one. This is due to the combined effect of the higher throat dimension and the lower chamber pressure peak of the Hippo 2 motor (see Fig.5), as there are practically no differences in terms of flame temperature and combustion products mass fractions (see Table 2).

In order to highlight the shape change effects captured by using subsequent steady-state CFD simulations, the erosion rate distributions obtained at the initial and final times have been made dimensionless in Fig. 8 with their respective nozzle throat values. It is immediately evident how shape change effects are more emphasized for the smaller motor (i.e., Hippo 1), as in this case nozzle erosion rate distribution shows to be more largely modified in the convergent and divergent zones. The reason is the different erosion level relatively to the nozzle dimension. In fact, according to the numerical results, the overall Hippo 1 and Hippo 2 nozzles throat erosion are respectively 26% and 12% relatively to the initial throat radius. Therefore, for the smaller motor (i.e., Hippo 1), the inclusion of shape change effects in the ablative simulations is more important. This is confirmed by looking to the final nozzle shapes reported in Fig.9. For the Hippo 2 motor, the final nozzle geometry and the axial translation of the throat section are approximately the same including or not including (i.e., using a single CFD simulation at average conditions) shape change effects in the CFD computations. On the other hand, for the Hippo 1 motor, the differences between the two approaches are more evident, with a different throat region translation and a substantially different final nozzle shape, especially in the convergent and divergent zones. For both motors considered, the numerical results are in good agreement with respect to experimental data all along the nozzle length. However, for Hippo 1 the numerical data overestimate the experimental erosion, while for Hippo 2 the numerical results are well inside the experimental uncertainty bar all along the nozzle length. The reasons of the overestimation for the Hippo 1 motor are expected to be possible heating transient effects, as in this case the firing duration (i.e., 29.5 seconds) is lower than in case of the Hippo 2 motor (i.e., 49.5 seconds) (see Fig.5(a)). In fact, the steady-state ablation assumption made in the CFD code becomes more and more acceptable as the firing duration is increased. Moreover, the overestimation in case of the Hippo 1 motor is different depending on the nozzle axial location, becoming higher in the convergent and divergent regions. In fact, in these regions the steady-state assumption becomes

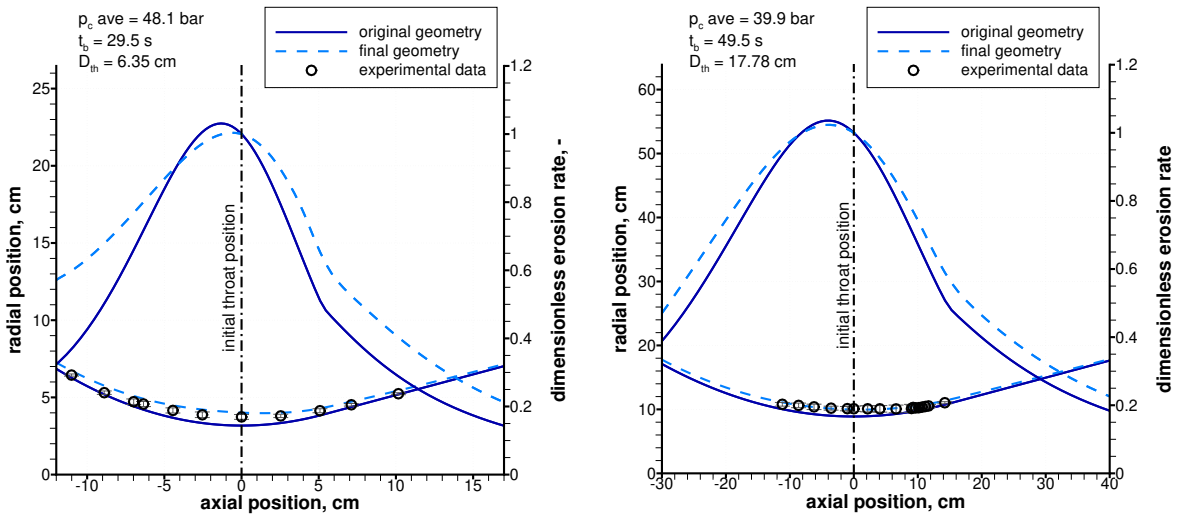

(b) Hippo 1. (c) Hippo 2.

Figure 8 Dimensionless erosion rate distributions along the nozzle length at the initial and final times for the two Hippo motors investigated and correspondent nozzle shapes.

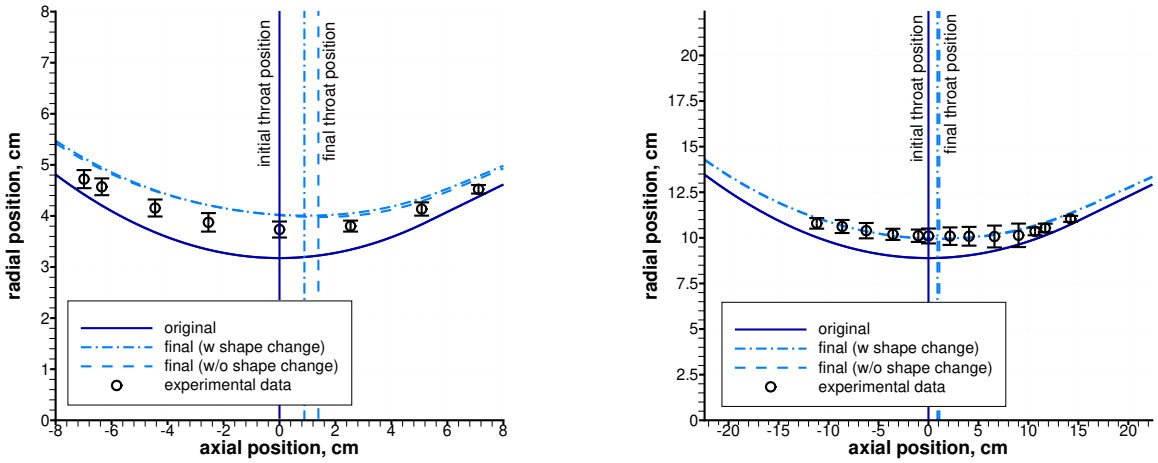

(a) Hippo 1. (b) Hippo 2.

Figure 9 Nozzle shape change according to the standalone steady-state CFD simulations approach and comparison with the experimental data for the two Hippo motors investigated.

less acceptable even if the firing duration is extremely long, as the convective heating rate is normally strongly reduced moving away from the throat region [41]. Therefore, transient heating effects need to be included in the numerical simulations in order to substantially improve the comparison with the experimental data.

B. CFD-PATO Results - Transient Heating and Ablation

In this section the CFD code has been loosely coupled to a three-dimensional material response code (i.e., PATO) in order to take into account transient heating effects in the nozzle erosion phenomenon. A simplified approach has been considered for the CFD-PATO coupling, as the main purpose of the analysis is to check the validity of the ablative

models for propulsive applications developed for PATO (i.e., the finite-rate B' ablation tables). In particular, a one-way coupling has been performed, using a single CFD simulation at average chamber pressure conditions in order to get the boundaries needed by PATO (see SectionII.B). These boundaries are kept constant for the whole firings duration. Both

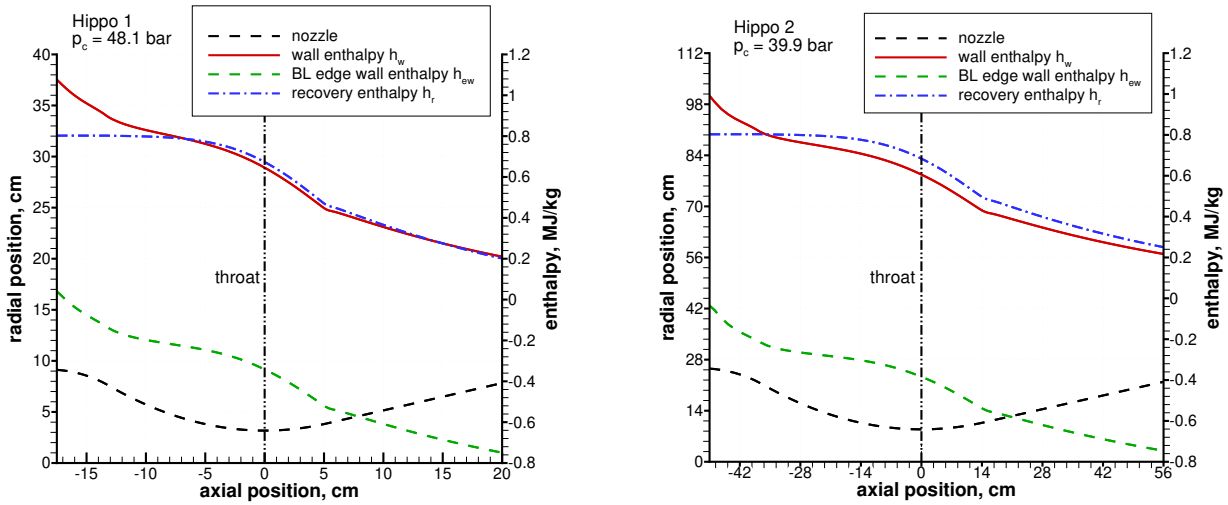

(a) Hippo 1.

(b) Hippo 2.

Figure 10 Wall, boundary-layer-edge wall, and recovery enthalpies distributions obtained from CFD simulations for both Hippo 1 and Hippo 2 nozzles.

Hippo 1 and Hippo 2 nozzles have been analyzed performing 2D axisymmetric CFD-PATO simulations, allowing the prediction of the nozzle shape change including transient heating effects.

1. PATO Boundaries

Before showing the CFD-PATO simulations results, the main CFD-derived data needed by PATO are shown and discussed. In Fig.10 enthalpies distributions are reported. The recovery enthalpy is needed by PATO for the resolution of the SEB (see Eq.(9)). In particular, recovery enthalpy has been obtained for the two nozzles performing adiabatic CFD simulations. Regarding wall and boundary-layer-edge wall enthalpies, they are needed for the calculation of the dimensionless mass and heat transfer coefficients (see Eq.(11)).

As thoroughly discussed in Section II.B, in this work PATO is employed under the typical assumption of unity Lewis number (Le), which, through the Chilton-Colburn relation, yields $C_M = C_H$. This is typically true in case of re-entry applications, for which material response code are widespread used. Here, the validity of the unity Lewis number assumption is checked for the specific SRM application aunder investigation (i.e., Hippo motor) by comparing the $\rho_e u_e C_H$ and $\rho_e u_e C_M$ distributions obtained from CFD (see Fig.11). It is worth noting how the resulting Lewis number is close to unity for most part of the nozzle length for both Hippo 1 and Hippo 2 nozzles, with the only exception of the upper convergent zone. Hence, results from the CFD-PATO simulations are expected to be not completely reliable only in the early convergent zone.

Finally, the equilibrium and finite-rate B' ablation tables and the wall enthalpy tables provided to PATO have been preliminarily checked against the steady-state ablative CFD solution at average chamber pressure conditions (see Figs.6 and 11). In particular, the B' parameters and the wall enthalpy calculated from CFD data at different nozzle locations have been qualitatively compared to the B' and wall enthalpy ablation tables. Results are summarized in Fig.12 for the Hippo 1 test case. Finite-rate B' and wall enthalpy ablation tables are almost perfectly superimposed to the steady-state CFD data. In particular, moving from nozzle convergent (red dots) towards nozzle throat (green dots), the finite-rate tables (red and green solid lines) are able to account for the slight reduction of the B' parameter due to surface reactions kinetic effects. On the other hand, the equilibrium ablation tables show some differences with respect to the CFD results. In particular, wall enthalpies are lower than the ones provided by the CFD code (see Fig.12(b)). For this reason, the steady-state wall temperature distribution resulting from the CFD-PATO simulations employing the equilibrium ablation tables is expected to be different from the CFD one. In particular, an higher wall temperature is needed in order to

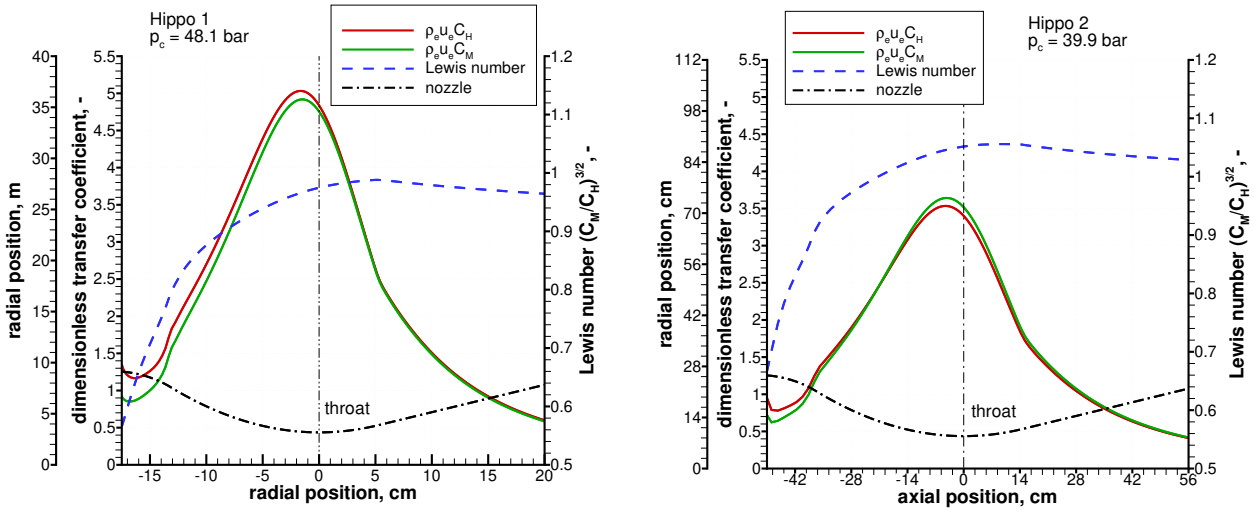

(a) Hippo 1.

(b) Hippo 2.

Figure 11 Dimensionless mass and heat transfer coefficients and correspondent Lewis number distributions all along the nozzle length for both Hippo 1 and Hippo 2.

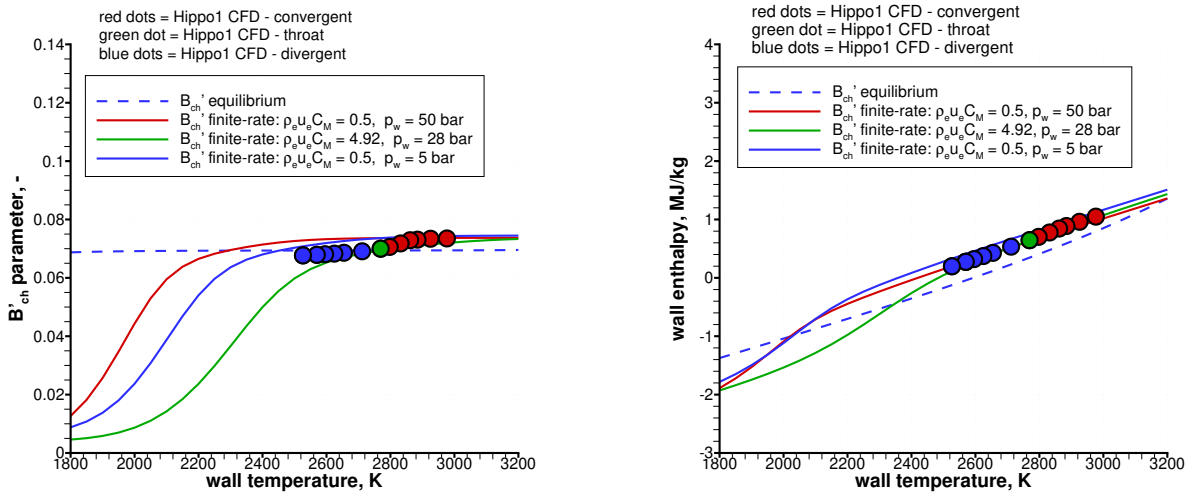

(a) B' parameter.

(b) Wall enthalpy.

Figure 12 Finite-rate and equilibrium B' ablation tables and wall enthalpy tables provided to PATO vs B'$_{ch}$ parameter and wall enthalpy computed from steady-state CFD simulations.

obtain the wall enthalpy computed by the CFD. From the results just shown, it is clear how the finite-rate ablation tables are expected to be more consistent with CFD simulations.

2. 2D-Axisym Results

Here, results obtained from 2D-axisymmetric CFD-PATO computations of the Hippo 1 and Hippo 2 nozzles, using both equilibrium and finite-rate ablation tables, are shown. The final purpose is the prediction of the nozzle shape change and of the char penetration depth during nozzles operation including transient heating effects.

First of all, the adoption of a back-wall adiabatic boundary condition in the CFD-PATO simulations has been checked

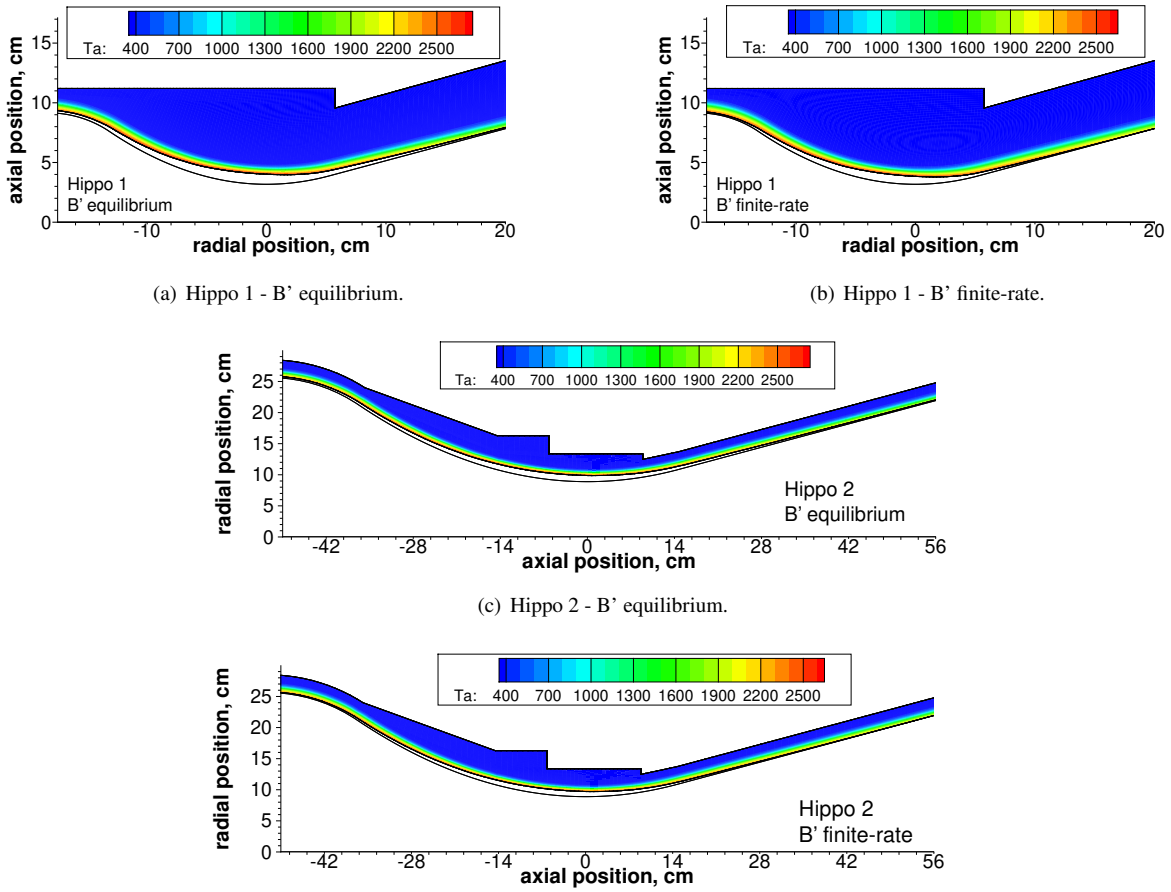

(a) Hippo 1 - B' equilibrium.

(b) Hippo 1 - B' finite-rate.

(c) Hippo 2 - B' equilibrium.

(d) Hippo 2 - B' finite-rate.

Figure 13 Temperature fields in the solid material at engine burn out from 2D-axisymmetric CFD-PATO simulations of the Hippo 1 and Hippo 2 motors using both equilibrium and finite-rate B' ablation tables.

by looking to the in-depth temperature fields inside the solid material (see Fig.13). As shown, the heat wave is not able to reach the back of the TPS in all cases. Hence, the adoption of an adiabatic boundary condition at the back-end of the TPS is totally justified. The heat penetration depth is quite uniform along the nozzle length, just slightly increasing in the divergent and convergent regions due to the lower erosion rate than at throat. In particular, for Hippo 1 nozzle the heat penetration depth at engine burn out is approximately 1.1 cm, 0.9 cm, and 1.15 cm at convergent inlet, throat, and divergent outlet, respectively. Slightly higher values of heat penetration depth are reported for the Hippo 2, nozzle, mainly due to its longer operation time and slightly lower erosion rates, with approximately 1.3, 1.1, and 1.35 cm at convergent inlet, throat, and divergent outlet, respectively. The heat penetration depth is just slightly affected by the particular B' ablation tables employed in PATO, leading to quite similar in-depth temperature fields inside the solid material for both motors (see Fig.13).

A detail of the in-depth material transient temperature and density profiles at throat for various times are shown in Fig.14 employing both equilibrium and finite-rate B' ablation tables. The heat penetration depth (with respect to the receding surface) after engine burn out is approximately 0.9 and 1.1 cm for Hippo 1 and Hippo 2 nozzles, respectively, independently from the particular ablation tables employed. Temperature profiles for various times obtained using the equilibrium and finite-rate ablation tables are qualitatively similar, with the only exception of the temperature values near the surface, which are lower in case of the finite-rate B' tables. In terms of material in-depth degradation due to the pyrolysis process, the material density variations through the thickness reflect those of a typical charring ablator, with values ranging from the virgin to the charred material density (i.e., from 1462 kg/m^3 to 1173 kg/m^3). Material charring is already taking place in the first second of exposure, reaching a maximum thickness of about 0.6 and 0.75 cm for Hippo 1 and Hippo 2 nozzles, respectively. Density variations alter the thermal diffusivity of the solid material, affecting the

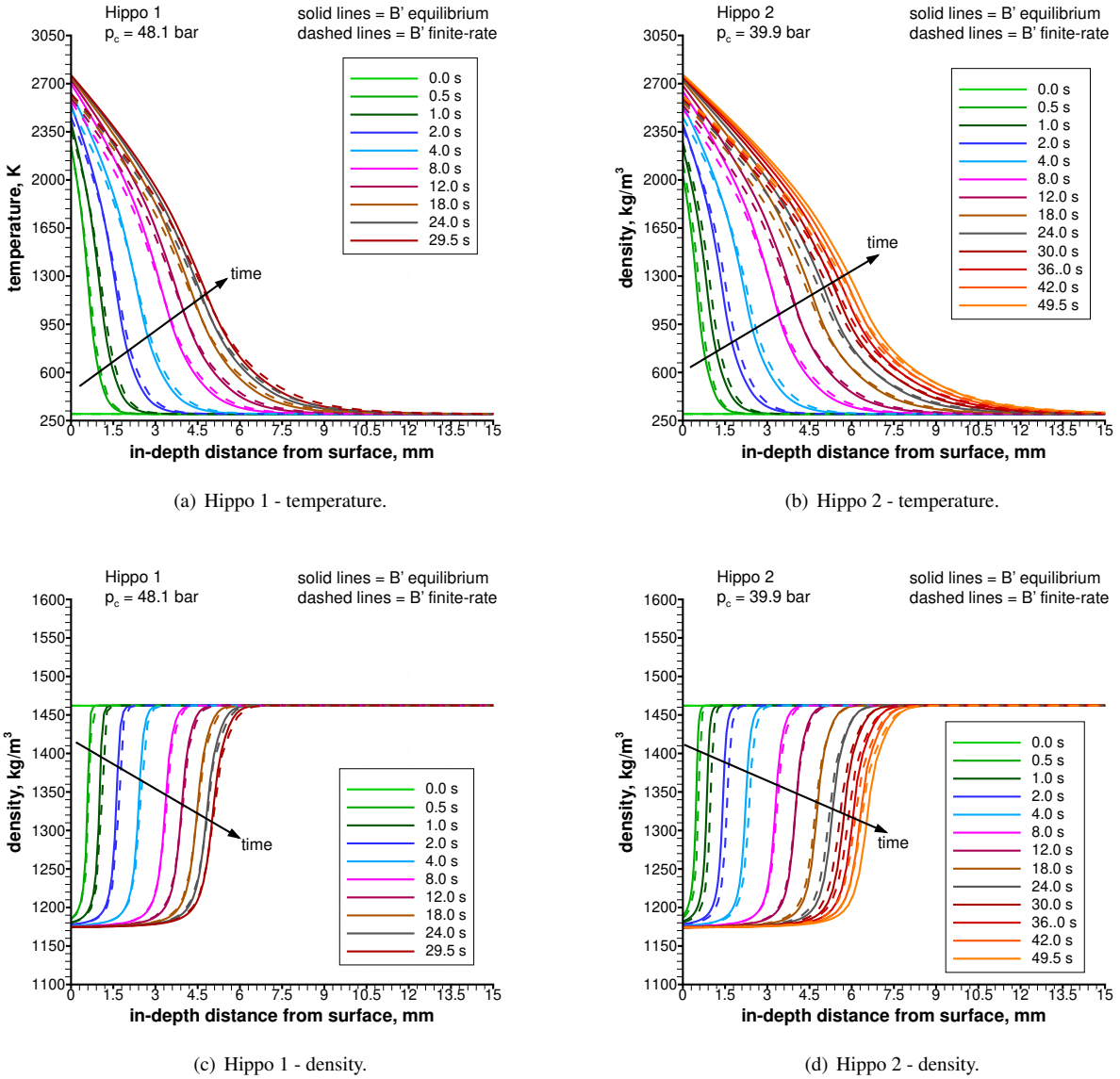

(a) Hippo 1 - temperature.

(b) Hippo 2 - temperature.

(c) Hippo 1 - density.

(d) Hippo 2 - density.

Figure 14 Temperature and density distributions in the solid material at throat for various times from 2D CFD-PATO simulations of the Hippo 1 and Hippo 2 motors using both equilibrium and finite-rate B' tables.

heat conduction process and leading to the slope variations in the temperature profiles shown in Figs.14(a) and 14(b).

Figure 15 shows the transient heat conduction solutions together with the CFD steady-state solution all along the nozzle length using both equilibrium and finite-rate B' ablation tables. Wall temperature in rapidly increasing in the first few seconds of operation in the throat section, where 2000 K are reached after less than one second of exposure. On the other hand, the temperature rise is slower in the nozzle regions away from the throat due to the lower heating rates (i.e., lower dimensionless heat transfer coefficients, see Fig.11). In particular, wall temperatures of 2000 K are reached in the whole convergent and divergent sections after approximately 2 to 4 seconds and 12 to 18 seconds, respectively, slightly varying depending on the ablation tables employed. In particular, nozzle heating is generally faster in the first seconds of exposure by using the finite-rate ablation tables. However, wall temperatures at engine burn out are higher when the equilibrium B' tables are employed. In this case, wall temperature at throat become even slightly higher than the correspondent CFD steady-state value (see Figs.15(a) and 15(c)). The reason is the substantial difference in ablation modeling between the CFD code, which employs a finite-rate heterogeneous gas-surface interaction model, and the

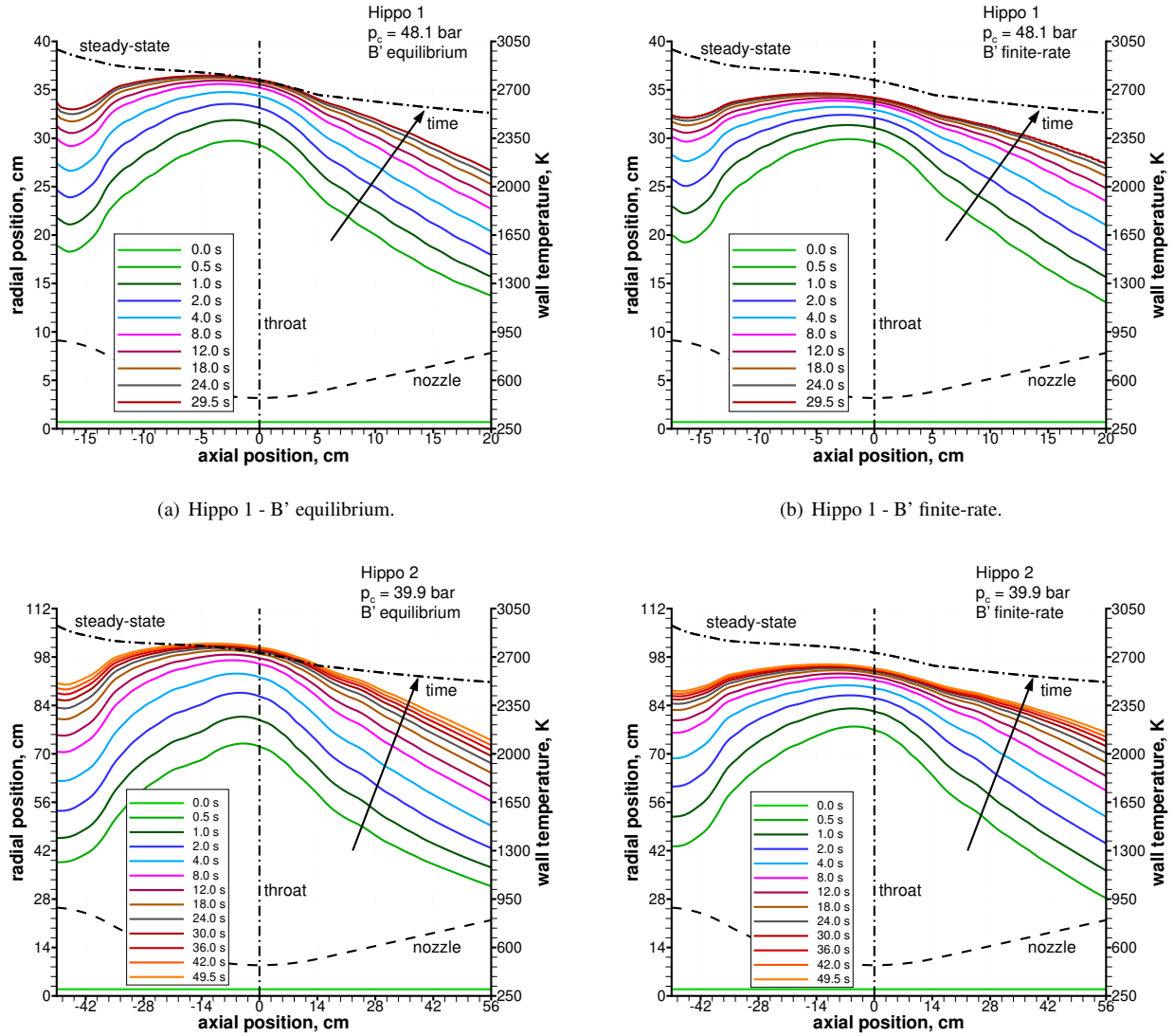

(a) Hippo 1 - B' equilibrium.

(b) Hippo 1 - B' finite-rate.

(c) Hippo 2 - B' equilibrium.

(d) Hippo 2 - B' finite-rate.

Figure 15 Wall temperature distributions for various time from 2D-axisymmetric CFD-PATO simulations of the Hippo 1 and Hippo 2 motors using both equilibrium and finite-rate B' ablation tables.

chemical equilibrium B' ablation tables used by PATO. In fact, as already observed, wall enthalpy tables computed under the chemical equilibrium hypothesis are not perfectly matching the CFD data (see Fig.12(b)), leading to a different steady-state surface heating. On the other hand, wall temperatures remain correctly always slightly lower than the correspondent CFD steady-state values when finite-rate ablation tables are used. In fact, in this case CFD and PATO ablation models are similar, as both take into account for finite-rate surface reactions effects (see Fig.12).

Figure 16 shows the B'_{ch} parameter along the nozzle obtained from CFD-PATO simulations for various times together with the steady-state one computed from CFD data according to Eq.(12). Concerning the Hippo 1 nozzle, substantially different results are reported depending on the particular ablation tables employed (see Figs.16(a) and 16(b)). In particular, in case the equilibrium B' tables are used, the B'_{ch} parameter is immediately reaching its maximum steady-state value (see Fig.16(a)). The absence of an actual transient phase is due to the behavior of the equilibrium B' tables (see Fig.3). In fact, when a wall temperature of approximately 1300-1500 K is reached, a plateau value for the equilibrium B' parameter is reached and surface ablation is not affected anymore by wall temperature variations. As

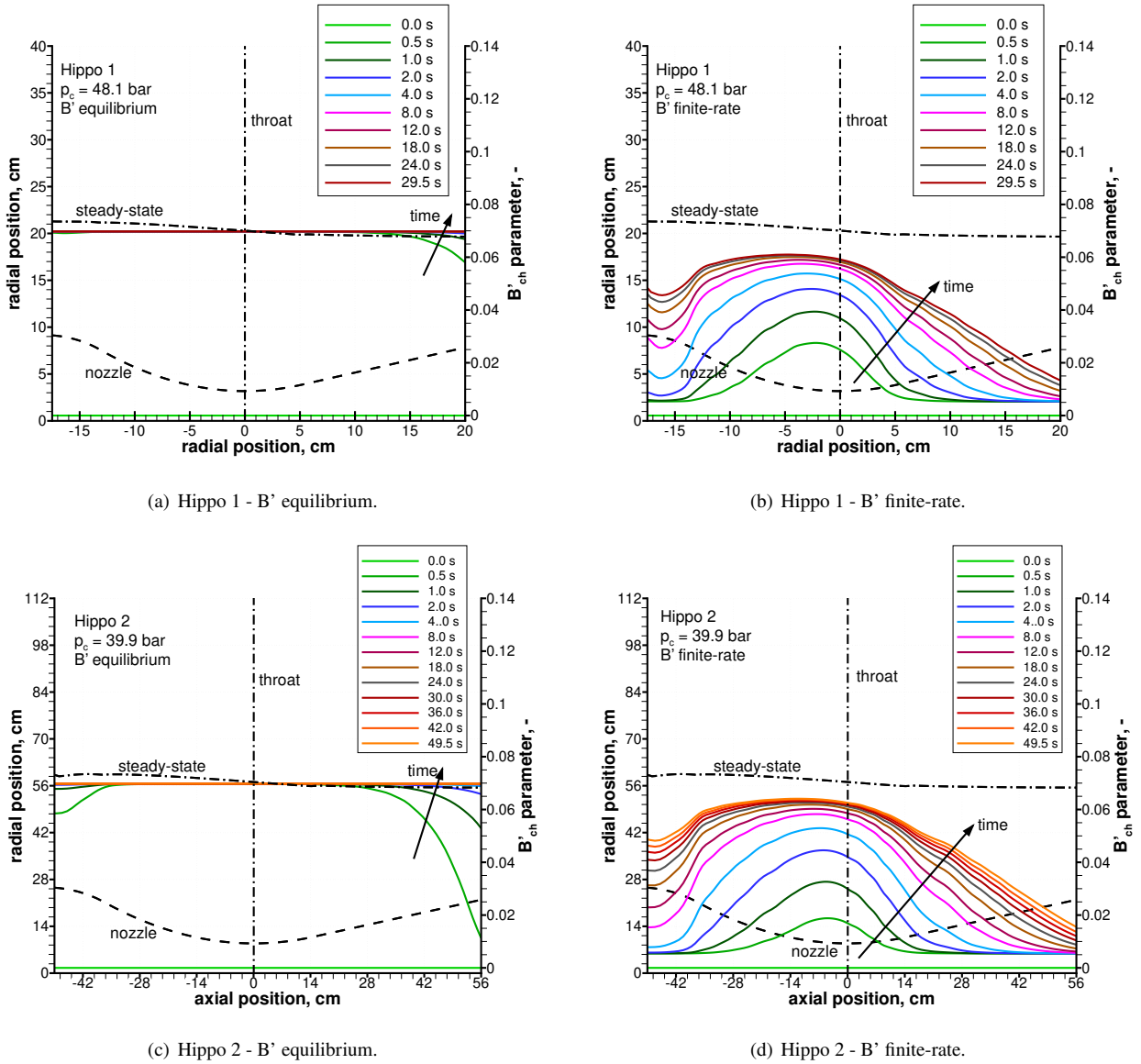

(a) Hippo 1 - B' equilibrium.

(b) Hippo 1 - B' finite-rate.

(c) Hippo 2 - B' equilibrium.

(d) Hippo 2 - B' finite-rate.

Figure 16 B'_{ch} parameter distributions for various time from 2D-axisymmetric CFD-PATO simulations of the Hippo 1 and Hippo 2 motors using both equilibrium and finite-rate B' ablation tables.

shown in Fig.15(a), a wall temperature of 1300-1500 K is reached in less than one second along the whole nozzle. The nozzle region experiencing the slower temperature rise is the nozzle divergent, where a slight in-time variation of the B'$_{ch}$ parameter can be observed in the first second of exposure. The absence of a transient phase for the B'$_{ch}$ parameter is an important limitation of the equilibrium B' tables as they are not able to take into account for the progressive increase of the surface reactions velocities leading to the transition from kinetic-limited to diffusion-limited ablation regimes. On the other hand, looking to the results obtained for the Hippo 1 nozzle employing the finite-rate B' ablation tables (see Fig.16(b), an evident transient phase can be observed. In particular, the B'$_{ch}$ parameter is rapidly increasing near the throat, while it grows slower moving towards the convergent and, more evidently, towards the divergent region. Similar results have been obtained for the Hippo 2 nozzle (see Figs.16(c) and 16(d)). However, in this case the the B'$_{ch}$ parameter is somehow slower in growing towards the steady-state, due to the lower average chamber pressure than Hippo 1 motor, leading to a reduced heating rate (i.e., a reduced dimensionless heat transfer parameter, see Fig.11).

The in-time behavior of the B'$_{ch}$ parameter is reflected by the obtained distributions of the char ablation mass

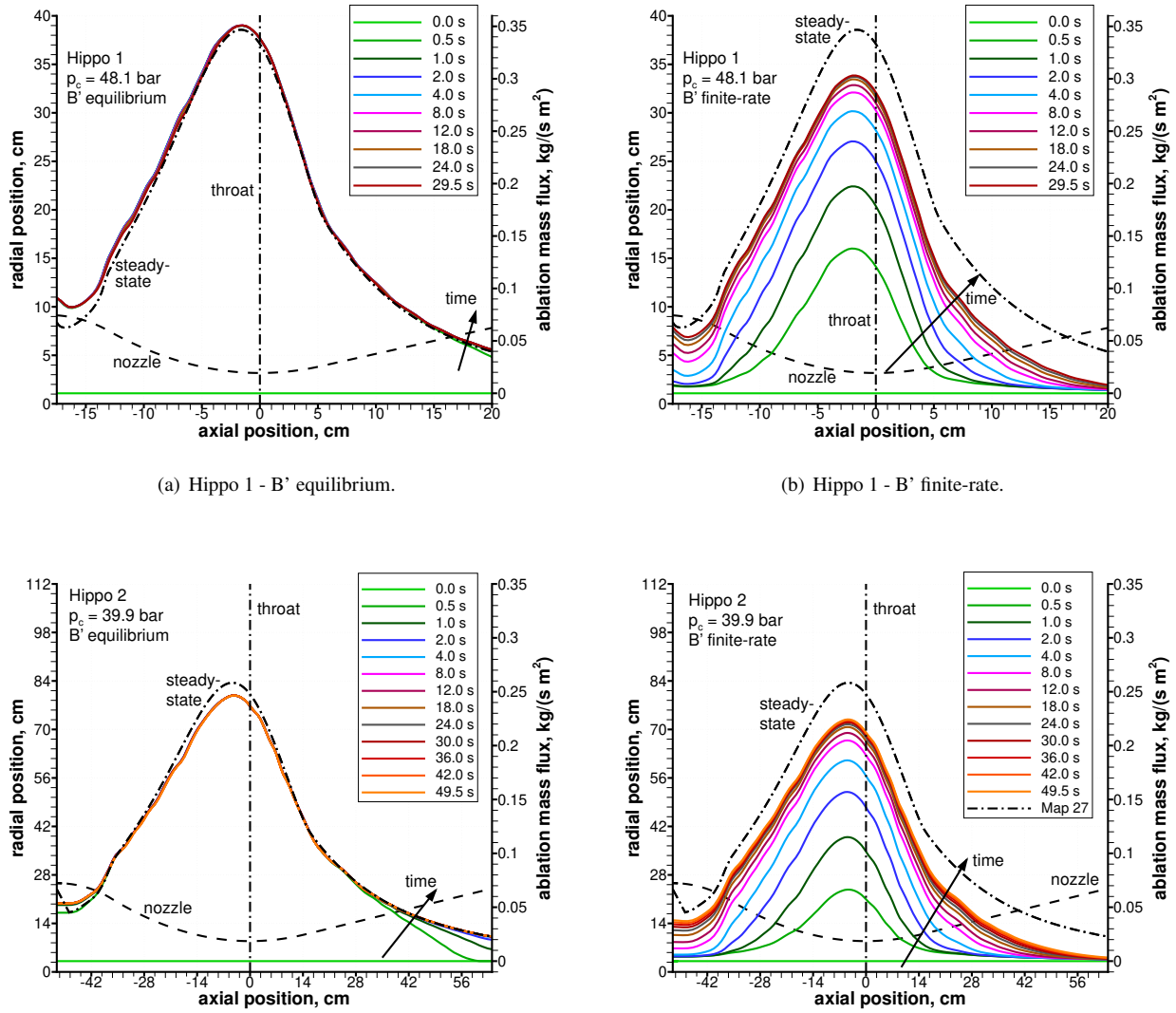

(a) Hippo 1 - B' equilibrium.

(b) Hippo 1 - B' finite-rate.

(c) Hippo 2 - B' equilibrium.

(d) Hippo 2 - B' finite-rate.

Figure 17 Char ablation mass flux $\dot{m}_{ch}$ distributions for various time from 2D-axisymmetric CFD-PATO simulations of the Hippo 1 and Hippo 2 motors using both equilibrium and finite-rate B' ablation tables.

flux reported in Fig.17. In case the equilibrium B' tables are used, char ablation mass flux immediately reaches the steady-state, with a barely noticeable transient phase in the divergent zone, more pronounced in case of the Hippo 2 nozzle, which is characterized by the lower chamber pressure. On the other hand, an evident transient phase is obtained by using the finite-rate B' ablation tables. Here, the different behaviors between the throat and the sections away from the throat is evident. In particular, there are sections in the divergent region extremely far from the steady-state and which are basically non-eroding for the whole firing duration. On the other hand, at throat the ablation mass flux at engine burn out is 83.8% and 87.0% of the correspondent steady-state value for the Hippo 1 and Hippo 2 nozzles, respectively. Moreover, the most important portion of the transient ablation phase at throat is taking place in the first 4 seconds of exposure, hence for the most part of motor firing nozzle throat ablation is quite close to the steady-state. Finally, concerning the convergent region, a faster transient phase than in the divergent region can be observed. However, results in the convergent portion of the nozzle are expected to be not completely reliable due to the non-unity Lewis number reported in this section of the nozzle (see Fig.11). The unreliability of the CFD-PATO result in the convergent

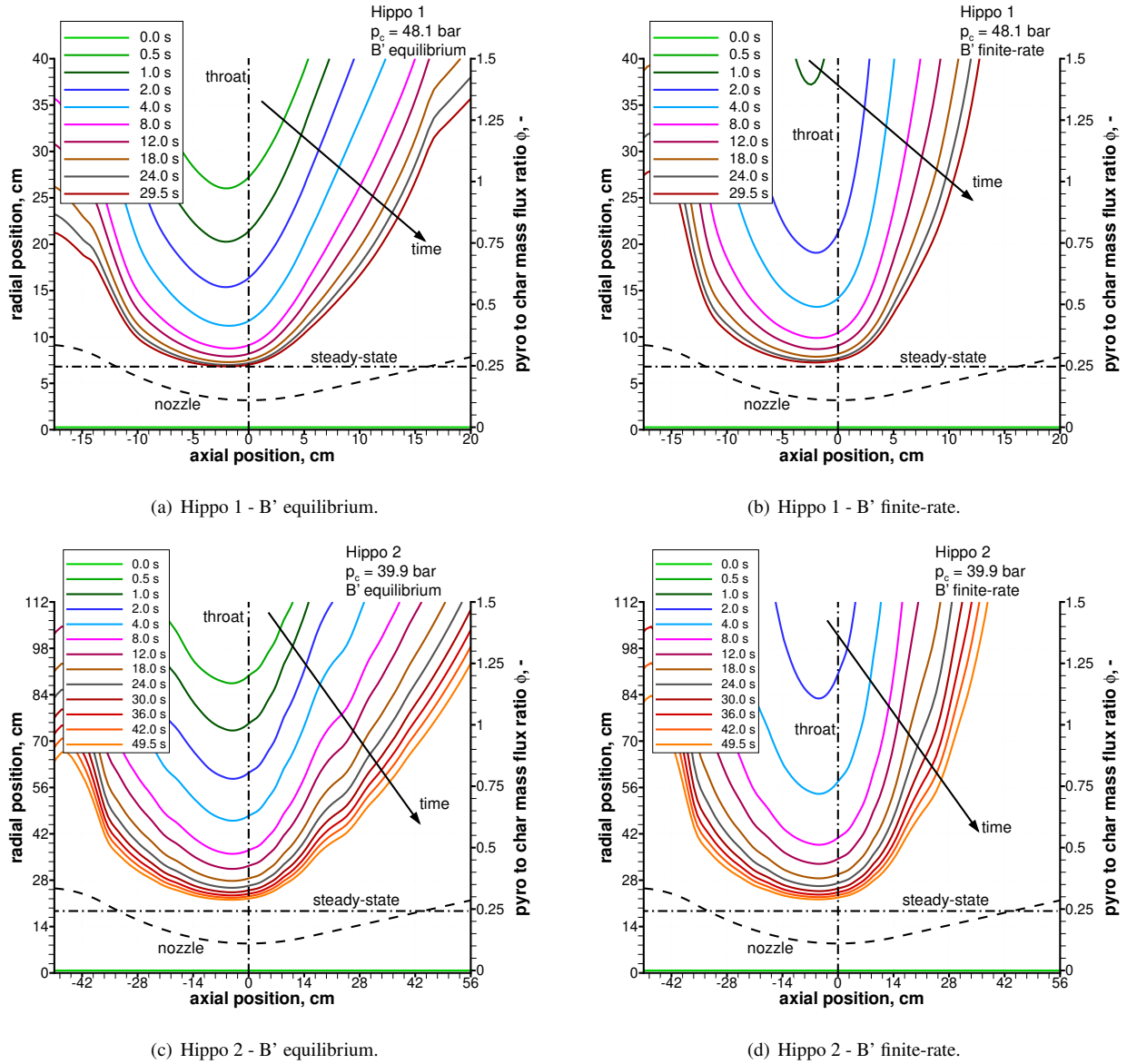

(a) Hippo 1 - B' equilibrium.

(b) Hippo 1 - B' finite-rate.

(c) Hippo 2 - B' equilibrium.

(d) Hippo 2 - B' finite-rate.

Figure 18 Pyro to char mass flux ratio distributions for various time from 2D-axisymmetric CFD-PATO simulations of the Hippo 1 and Hippo 2 motors using both equilibrium and finite-rate B' ablation tables.

region is evident looking to the results obtained employing the equilibrium B' ablation tables (see Figs.17(a) and 17(c)). In fact, in the early convergent regions char ablation mass flux is overestimated if compared to the steady-state CFD one. The reason is the Lewis number being lower than unity (see Fig.11), meaning that the dimensionless heat transfer coefficient (which is the one given to PATO as boundary condition) is here actually higher than the correspondent dimensionless mass transfer coefficien. It is worth noting how Lewis number becomes slightly higher than unity for Hippo 2 nozzle around the throat region (see Fig.11(b)). In this case the opposite is taking place, with char ablation mass flux from CFD-PATO simulation underestimating the CFD one, as evident in Fig.17(c).

Figure 18 shows the pyrolysis to char mass flux ratio ϕ along the nozzle at various time together with its steady-state theoretical value. The throat region is the only one approaching the steady-state after approximately 8 and 18 seconds of exposure for Hippo 1 and Hippo 2 nozzles, respectively. On the other hand, divergent and convergent nozzle zones remains quite far from being at steady-state. Moreover, ϕ is somehow slower in moving towards the steady solution in case finite-rate ablation tables are employed. In fact, while in-depth pyrolysis is almost immediately taking place

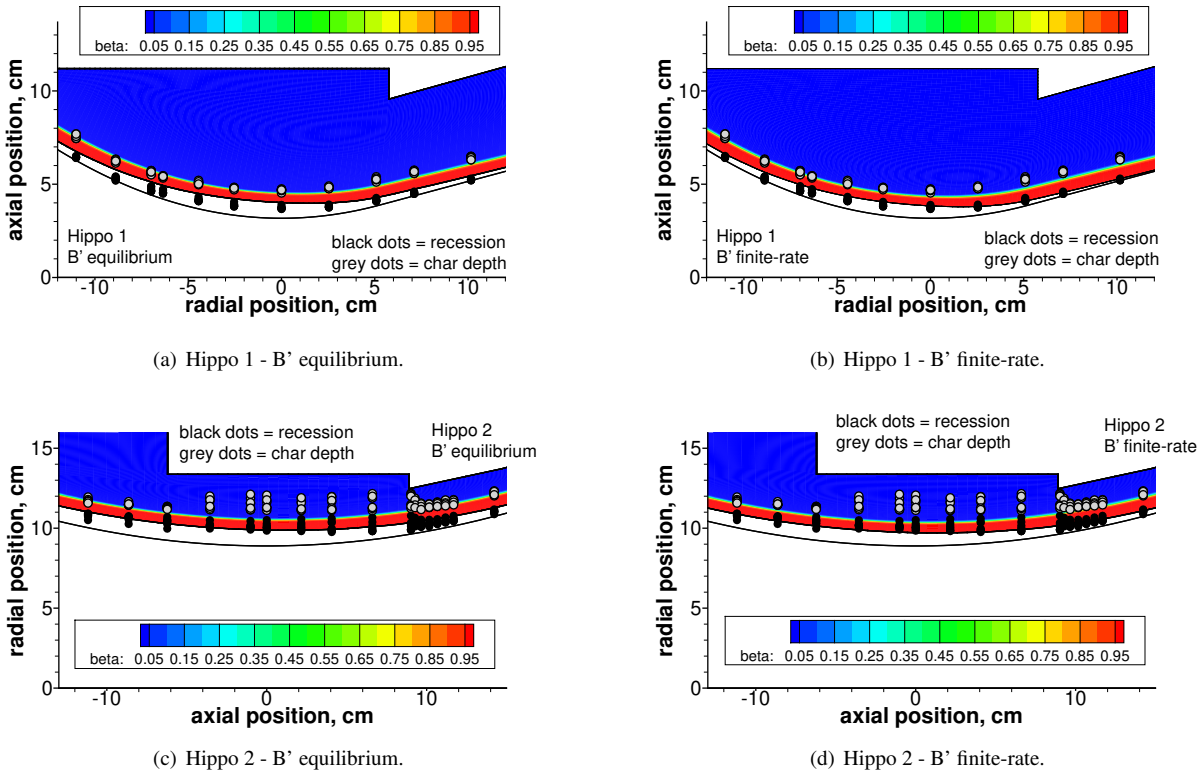

(a) Hippo 1 - B' equilibrium.

(b) Hippo 1 - B' finite-rate.

(c) Hippo 2 - B' equilibrium.

(d) Hippo 2 - B' finite-rate.

Figure 19 Pyrolysis progress parameter fields and comparison between experimental and computed char penetration depth for Hippo 1 and Hippo 2 motors using both equilibrium and finite-rate B' ablation tables.

independently from the particular B' tables employed in PATO (see in-depth density distributions shown in Fig.14(c) and 14(d)), char ablation at surface shows a different in-time behavior by using equilibrium or finite-rate ablation tables (see Fig.17).

Figure 19 shows the comparison between the calculated and experimentally measured char penetration depth along the nozzles. In particular, the pyrolysis progress parameter β is shown, which is defined as:

$$\beta = \frac{\rho_v - \rho}{\rho_v - \rho_{ch}} \tag{18}$$

Therefore, a zero β value means the material density is equal to the virgin one, ρ_v, hence no in-depth decomposition has still taken place, while a unitary β value means the material density is the charred one, ρ_{ch}, meaning that the pyrolysis process has been completed. Regarding the Hippo 1 nozzle (see Figs.19(a) and 19(b)), char penetration depth data are in good agreement with the available experimental data, with the only exception of the divergent region, where char penetration depth is slightly overestimated. Regarding Hippo 2 nozzle (see Figs.19(c) and 19(d)), the available experimental data shows to be quite scattered. The reason is the presence of irregular surface erosion, especially in the throat region, which may be due to possible mechanical spallation. However, in the convergent and divergent zones, characterized by less experimental uncertainty (i.e., no evidences of mechanical erosion), the numerical results shows to be in very good agreement with the experimental data. This is particularly evident in the divergent, where a lot of experimental measurements are available. Qualitatively, no differences in terms of char penetration depth can be reported in case equilibrium or finite-rate B' ablation tables are employed in PATO.

Lastly, Fig. 20 shows the final nozzle shapes obtained for the two Hippo nozzles under investigation using CFD-PATO simulations employing both equilibrium and finite-rate ablation tables. These shapes have been compared with the one previously obtained using standalone CFD simulations (see Fig.9), trying to highlight possible improvements with respect to the available experimental data. Concerning Hippo 1 nozzle, the adoption of the CFD-PATO simulations allows to drastically improve the agreement with the experimental data all along the nozzle in case the finite-rate ablation tables are used. In fact, in this case the nozzle erosion transient phase is correctly taken into account. In particular, the

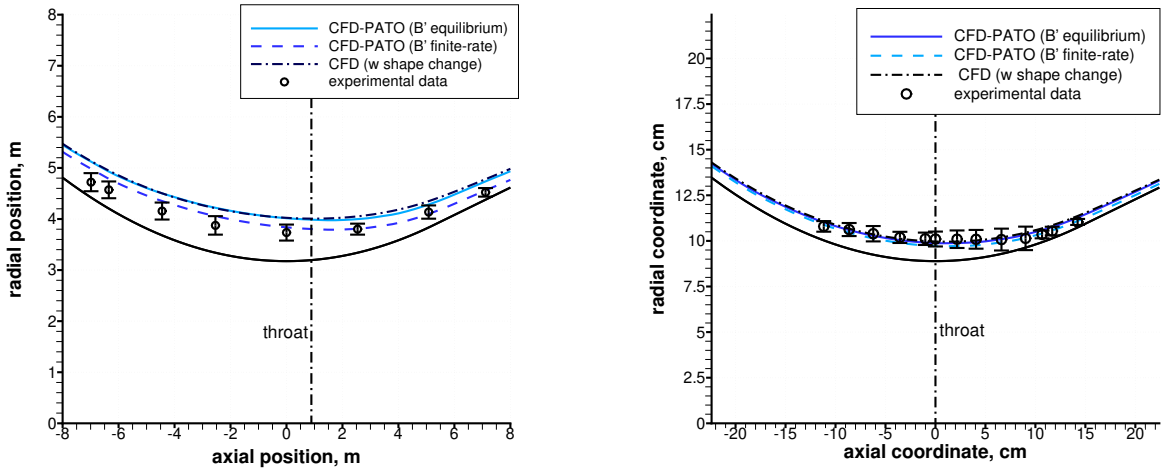

(a) Hippo 1.

(b) Hippo 2.

Figure 20 Nozzle shape change according to CFD-PATO simulations using both equilibrium and finite-rate B' ablation tables and according to subsequent steady-state CFD simulations and comparison with the experimental data.

larger improvement with respect to the standalone CFD simulations has been obtained in the divergent zone, in which nozzle erosion is quite low. On the other hand, the final nozzle shape resulting from CFD-PATO simulations employing the equilibrium B' table is substantially superimposed to the standalone CFD one. The reason is the lack of an actual transient erosion phase using the equilibrium tables in PATO (see Fig.17(a)), resulting in no improvements with respect to the steady-state CFD. On the other hand, regarding Hippo 2 nozzle, there are no evident improvements by employing the CFD-PATO approach with respect to the experimental data, with the only exception of the divergent region when finite-rate ablation tables are used. In fact, the CFD-PATO simulations employing the finite-rate B' tables are the only one able to take into account for the extremely slow ablation mass flux increment with time in the divergent region (see Figs.17(b) and 17(d)), which seems to be confirmed from the experimental data for both Hippo 1 and Hippo 2 nozzles. Anyway, at throat the numerical results show to be in good agreement with the experimental measurements in case of both CFD and CFD-PATO simulations, with the overall erosion not largely varying. The reason is the longer duration of the motor firing in case of the Hippo 2 nozzle, making the assumption of steady-state ablation more reasonable, especially at throat. Hence, from a point of view of motor design (i.e., throat erosion prediction), steady-state CFD simulations proved to be a reasonable approach in case of long firing duration. On the contrary, transient effects must be carefully taken into account when throat erosion of short duration motors have to be predicted, or in case nozzle ablation and heating in the convergent and divergent regions of the nozzle need to be analyzed.

V. Conclusion

In this work nozzle heating, pyrolysis, and shape change have been investigated for two different sub-scale Space Shuttle solid propellant booster nozzles using both steady-state CFD and transient CFD-PATO simulations.

Nozzle heating and shape change have been firstly analyzed by using standalone steady-state CFD simulations. The obtained results have shown how CFD is in good agreement with the available experimental data in case of a long duration motor firing, for which the steady-state assumption appears to be reasonable. On the other hand, for a short duration motor, CFD data overestimates surface erosion all along the nozzle length. In particular, erosion overestimation has shown to be low at nozzle throat, increasing moving towards the convergent and divergent regions, in which transient effects are expected to be more relevant. Regarding shape change effects on the nozzle erosion process, they have been observed to be more emphasized in case of smaller nozzle dimensions. In this case the initial throat diameter is lower relatively to the nozzle erosion rate, leading to stronger time variations of the area ratio in the convergent and divergent zones, affecting more the nozzle erosion process over time.

The assumption of unity Lewis number made in PATO, typically valid concerning re-entry applications, has been checked for the particular propulsive test case considered looking to CFD data. The hypothesis has shown to be extremely reasonable in the throat and divergent nozzle regions. However, in the convergent zone the Lewis number has shown to be sensibly lower than unity, leading to possible inconsistencies in the CFD-PATO simulations. This has been confirmed from the obtained results, with ablation mass fluxes in the convergent region higher than the steady-state CFD one in case the equilibrium B' tables are employed in the material response code. Hence, the relaxation of the unitary Lewis number hypothesis in PATO can be of importance in order to correctly handle nozzle ablation and shape change in the nozzle convergent region.

Both equilibrium and finite-rate thermochemical B' ablation tables have been computed for the specific propulsive application considered. Then, CFD-PATO simulations have been carried out in order to check the validity and consistency of the derived B' tables. The obtained results underlined how practically no transient erosion effects can be captured along the whole nozzle if the chemical equilibrium B' tables are used. In fact, the equilibrium B' tables are not able to take into account for the progressive increase of the surface reactions velocities leading to the transition from kinetic-limited to diffusion-limited ablation regimes as wall temperature rises. On the other hand, this is taken into account by using finite-rate B' ablation tables. The available experimental data in terms of nozzle erosion for the short duration motor have been overestimated by the CFD-PATO simulations using the equilibrium B' ablation tables, with results similar to the standalone CFD. Instead, the agreement with the experimental measurements all along the nozzle has been largely enhanced employing the finite-rate B' tables thanks to the correct prediction of the transient erosion phase. In particular, an almost null erosion has been predicted in the nozzle divergent, as confirmed from the experiments.

It is worth noting how the CFD steady-state ablative simulations carried out in this work lack in terms of material pyrolysis and pyrolysis-boundary layer gases interaction modeling. Hence, a future development of this work will be the inclusion of nozzle pyrolysis in the ablative CFD simulations. Moreover, the CFD-PATO simulations have been carried out in a simplified manner, using a single CFD simulation and without an effective tight coupling between the two codes. Therefore, a future development of this work will be the establishment of a more accurate coupling strategy, allowing for the exchange of different parameters, such as nozzle shape, pyrolysis ablation mass flux, and conductive heat flux distributions, between the two codes. In this way, shape change, transient heating and pyrolysis effects can be more rigorously taken into account.

Acknowledgments

This work has been partially funded within the project no. ARS01_01318 - Generazione E - of the Italian Ministry of University and Research.

References

[1] Kendall, R., Rindal, R., Moyer, C., and Bartlett, E., "User's Manual: Aerotherm Charring Material Thermal Response and Ablation Program - Version 3," Tech. Rep. AD875062, AFRPL, 1970.

[2] Thakre, P., and Yang, V., "Chemical Erosion of Carbon-Carbon/Graphite Nozzles in Solid-Propellant Rocket Motors," *Journal of Propulsion and Power*, Vol. 24, No. 4, 2008, pp. 822–833. https://doi.org/10.2514/1.34946.

[3] Bianchi, D., Nasuti, F., and Martelli, E., "Coupled Analysis of Flow and Surface Ablation in Carbon-Carbon Rocket Nozzles," *Journal of Spacecraft and Rockets*, Vol. 46, No. 3, 2009, pp. 492–500. https://doi.org/10.2514/1.40197.

[4] Bianchi, D., and Nasuti, F., "Numerical Analysis of Nozzle Material Thermochemical Erosion in Hybrid Rocket Engines," *Journal of Propulsion and Power*, Vol. 29, No. 3, 2013, pp. 547–558. https://doi.org/10.2514/1.B34813.

[5] Bianchi, D., Nasuti, F., Paciorri, R., and Onofri, M., "Hypersonic Flow Anlysis Including Finite Rate Ablation Thermochemistry," *EUCASS conference*, 2013.

[6] Lachaud, J., Magin, T. E., Cozmuta, I., and Mansour, N. N., "A Short Review of Ablative-Material Response Models and Simulation Tools," *7th European Symposium on Aerothermodynamics*, 2011.

[7] Olynick, D., Chen, Y.-K., and Tauber, M. E., "Aerothermodynamics of the Stardust Sample Return Capsule," *Journal of Spacecraft and Rockets*, Vol. 36, No. 3, 1999, pp. 442–462. https://doi.org/10.2514/2.3466.

[8] Chen, Y.-K., Milos, F. S., and Gokcen, T., "Loosely Coupled Simulation for Two-Dimensional Ablation and Shape Change," *Journal of Spacecraft and Rockets*, Vol. 47, No. 5, 2010, pp. 775–785. https://doi.org/10.2514/1.39667.

[9] Chen, Y.-K., and Gokçen, T., "Effect of Nonequilibrium Surface Thermochemistry in Simulation of Carbon-Based Ablators," *Journal of Spacecraft and Rockets*, Vol. 50, No. 5, 2013, pp. 917–926. https://doi.org/10.2514/1.A32451.

[10] Farbar, E. D., Alkandry, H., Wiebenga, J., and Boyd, I. D., "Simulation of Ablating Hypersonic Vehicles with Finite-Rate Surface Chemistry," *AIAA*, paper 2014-2124, 2014. https://doi.org/10.2514/6.2014-2124.

[11] Martin, A., and Boyd, I. D., "Strongly Coupled Computation of Material Response and Nonequilibrium Flow for Hypersonic Ablation," *Journal of Spacecraft and Rockets*, Vol. 52, No. 1, 2015, pp. 89–104. https://doi.org/10.2514/1.A32847.

[12] Cross, P. G., and Boyd, I. D., "Conjugate Analyses of Ablation in Rocket Nozzles," *Journal of Spacecraft and Rockets*, Vol. 56, No. 5, 2019, pp. 1593–1610. https://doi.org/10.2514/1.A34311.

[13] Cross, P. G., "Coupled Simulations of Finite-Rate Ablation with Pyrolysis in Rocket Nozzles," *Journal of Thermophysics and Heat Transfer*, Vol. 34, No. 2, 2020, pp. 381–392. https://doi.org/10.2514/1.T5860.

[14] Kamps, L., Hirai, S., Sakurai, K., Viscor, T., Saito, Y., Guan, R., Isochi, H., Adachi, N., Itoh, M., and Nagata, H., "Investigation of Graphite Nozzle Erosion in Hybrid Rockets Using Oxygen/High-Density Polyethylene," *Journal of Propulsion and Power*, Vol. 36, No. 3, 2020, pp. 423–434. https://doi.org/10.2514/1.B37568.

[15] Bianchi, D., Migliorino, M. T., Rotondi, M., Kamps, L., and Nagata, H., "Numerical Analysis of Nozzle Erosion in Hybrid Rockets and Comparison with Experiments," *Journal of Propulsion and Power*, 2021, pp. 1–22. https://doi.org/10.2514/1.B38547, articles in advance.

[16] Rotondi, M., Migliorino, M. T., Bianchi, D., Kamps, L. T., and Nagata, H., "Numerical Analysis of Nozzle Transient Heating and Erosion in Hybrid Rockets burning HDPE," *AIAA*, paper 2021-3496, 2021. https://doi.org/10.2514/6.2021-3496.

[17] Migliorino, M. T., Bianchi, D., and Nasuti, F., "Gas-Phase Reaction Effects on Nozzle Erosion in Paraffin/Oxygen Hybrid Rockets," *AIAA*, paper 2021-3494, 2021. https://doi.org/10.2514/6.2021-3494.

[18] Lachaud, J., and Mansour, N. N., "Porous-Material Analysis Toolbox Based on OpenFOAM and Applications," *Journal of Thermophysics and Heat Transfer*, Vol. 28, No. 2, 2014, pp. 191–202. https://doi.org/10.2514/1.T4262.

[19] Meurisse, J. B., Lachaud, J., Panerai, F., Tang, C., and Mansour, N. N., "Multidimensional material response simulations of a full-scale tiled ablative heatshield," *Aerospace Science and Technology*, Vol. 76, 2018, pp. 497–511. https://doi.org/https://doi.org/10.1016/j.ast.2018.01.013.

[20] Rotondi, M., Migliorino, M. T., Bianchi, D., Pagani, P., and Turchi, A., "Numerical and Experimental Analysis of Capsules Ablation and Shape Change including Heating Transient Effects," *AIAA*, paper 2020-3969, 2020. https://doi.org/10.2514/6.2020-3969.

[21] Arnold, J., Dodson, J., and Laub, B., "Subscale Solid Motor Nozzle Tests (Phase IV), and Nozzle Materials Screening and Thermal Characterization (Phase V)," Tech. Rep. CR 161254, NASA, 1979.

[22] Bianchi, D., Nasuti, F., Martelli, E., and Onofri, M., "A Numerical Approach for High-Temperature Flows over Ablating Surfaces," *AIAA*, paper 2007-4537, 2007. https://doi.org/10.2514/6.2007-4537.

[23] Bianchi, D., Nasuti, F., Onofri, M., and Martelli, E., "Thermochemical Erosion Analysis for Graphite/Carbon-Carbon Rocket Nozzles," *Journal of Propulsion and Power*, Vol. 27, No. 1, 2011, pp. 197–205. https://doi.org/10.2514/1.47754.

[24] Bianchi, D., and Nasuti, F., "Numerical Analysis of Nozzle Material Thermochemical Erosion in Hybrid Rocket Engines," *Journal of Propulsion and Power*, Vol. 29, No. 3, 2013, pp. 547–558. https://doi.org/10.2514/1.B34813.

[25] Turchi, A., Bianchi, D., Nasuti, F., and Onofri, M., "A Numerical Approach for the Study of the Gas-Surface Interaction in Carbon-Phenolic Solid Rocket Nozzles," *Aerospace Science and Technology*, Vol. 27, No. 1, 2013, pp. 25–31. https://doi.org/10.1016/j.ast.2012.06.003.

[26] Bianchi, D., Turchi, A., Nasuti, F., and Onofri, M., "Chemical Erosion of Carbon-Phenolic Rocket Nozzles with Finite-Rate Surface Chemistry," *Journal of Propulsion and Power*, Vol. 29, No. 5, 2013, pp. 1220–1230. https://doi.org/10.2514/1.B34791.

[27] Bianchi, D., Migliorino, M. T., Nasuti, F., and Onofri, M., "CFD Analysis of Paraffin-Based Hybrid Rockets with Coupled Nozzle Erosion Characterization," *AIAA*, paper 2019-4263, 2019. https://doi.org/10.2514/6.2019-4263.

[28] Bianchi, D., Nasuti, F., and Onofri, M., "Radius of Curvature Effects on Throat Thermochemical Erosion in Solid Rocket Motors," *Journal of Spacecraft and Rockets*, Vol. 52, No. 2, 2015, pp. 320–330. https://doi.org/10.2514/1.A32944.

[29] Bianchi, D., and Nasuti, F., "Navier–Stokes Simulation of Graphite Nozzle Erosion at Different Pressure Conditions," *AIAA Journal*, Vol. 53, No. 2, 2015, pp. 356–366. https://doi.org/10.2514/1.J053154.

[30] Bianchi, D., and Neri, A., "Numerical Simulation of Chemical Erosion in Vega Solid-Rocket-Motor Nozzles," *Journal of Propulsion and Power*, Vol. 34, No. 2, 2018, pp. 482–498. https://doi.org/10.2514/1.B36388.

[31] Bianchi, D., and Nasuti, F., "Carbon-Carbon Nozzle Erosion and Shape-Change Effects in Full-Scale Solid-Rocket Motors," *Journal of Propulsion and Power*, Vol. 28, No. 4, 2012, pp. 820–830. https://doi.org/10.2514/1.B34267.

[32] Lachaud, J., Scoggins, J., Magin, T., Meyer, M., and Mansour, N., "A generic local thermal equilibrium model for porous reactive materials submitted to high temperatures," *International Journal of Heat and Mass Transfer*, Vol. 108, No. B, 2017, pp. 1406–1417. https://doi.org/10.1016/j.ijheatmasstransfer.2016.11.067.

[33] Lachaud, J., and Mansour, N., "Porous-Material Analysis Toolbox Based on OpenFOAM and Applications," *Journal of Thermophysics and Heat Transfer*, Vol. 28, No. 2, 2014, pp. 191–202. https://doi.org/10.2514/1.T4262.

[34] Lachaud, J., Magin, T. E., Cozmuta, I., and Mansour, N., "A Short Review of Ablative-Material Response Models and Simulation Tools," *7th aerothermodynamics symposium, ESA*, 2011.

[35] Omidy, A., Panerai, F., Martin, A., Lechaud, J., Cozmuta, I., and Mansour, N., "Code-to-Code Comparison, and Material Response Modeling of Stardust and MSL using PATO and FIAT," Tech. Rep. NASA/CR-2015-218960, NASA, 2015.

[36] Lachaud, J., van Eekelen, T., Scoggins, J., Magin, T., and Mansour, N., "Detailed Chemical Equilibrium Model for Porous Ablative Materials," *International Journal of Heat and Mass Transfer*, Vol. 90, 2015, pp. 1034–1045. https://doi.org/10.1016/j.ijheatmasstransfer.2015.05.106.

[37] Bradley, D., Dixon-Lewis, G., din Habik, S. E., and Mushi, E., "The oxidation of graphite powder in flame reaction zones," *Symposium (International) on Combustion*, Vol. 20, No. 1, 1985, pp. 931 – 940. https://doi.org/https://doi.org/10.1016/S0082-0784(85)80582-8.

[38] Chelliah, H., Makino, A., Kato, I., Araki, N., and Law, C., "Modeling of graphite oxidation in a stagnation-point flow field using detailed homogeneous and semiglobal heterogeneous mechanisms with comparisons to experiments," *Combustion and Flame*, Vol. 104, No. 4, 1996, pp. 469–480. https://doi.org/10.1016/0010-2180(95)00151-4.

[39] Gordon, S., and McBride, B. J., "Computer Program for Calculation of Complex Chemical Equilibrium Compositions and Applications," Tech. Rep. RP-1311, NASA, 1994.

[40] Bianchi, D., Migliorino, M. T., Rotondi, M., Kamps, L. T., and Nagata, H., "Numerical Analysis of Nozzle Heating and Erosion in Hybrid Rockets and Comparison with Experiments," *AIAA Propulsion and Energy 2020 Forum*, 2020. https://doi.org/10.2514/6.2020-3767.

[41] Bianchi, D., Turchi, A., Nasuti, F., and Onofri, M., "Coupled CFD Analysis of Thermochemical Erosion and Unsteady Heat Conduction in Solid Rocket Nozzles," *AIAA*, paper 2012-4318, 2012. https://doi.org/10.2514/6.2012-4318.